NASA Technical Memorandum 110252
U. S. Army Research Laboratory Memorandum Report 328

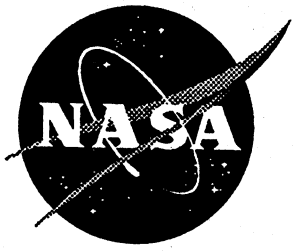

AN AEROELASTIC ANALYSIS OF HELICOPTER ROTOR BLADES INCORPORATING PIEZOELECTRIC FIBER COMPOSITE TWIST ACTUATION

W. Keats Wilkie
Vehicle Structures Directorate
U.S. Army Research Laboratory
Langley Research Center, Hampton, Virginia

K. C. Park
University of Colorado, Boulder, Colorado

May 1996

National Aeronautics and
Space Administration
Langley Research Center
Hampton, Virginia 23681-0001

CONTENTS

NOMENCLATURE

A	rotor disk area, πR^2, or spar material cross sectional area, in^2
A_e	thin-walled spar section enclosed area, in^2
a	lift curve slope, rad^{-1}
b	blade semichord, c/2, in
$\bar{b}$	normalized blade semichord, b/R
c	blade chord, in
$\bar{c}$	normalized blade chord, c/R
C_T	rotor thrust coefficient, $C_T = T/\rho A\Omega^2 R^2$
C_m	section pitching moment coefficient, $C_m = M_\theta / \frac{1}{2}\rho V^2 c^2$
$C_{m\ell}$	linear model static pitching moment coefficient
C_{ms}	measured static pitching moment coefficient
C_z	section lift coefficient, $C_z = L_z / \frac{1}{2}\rho V^2 c$
$C_{z\ell}$	linear model static lift coefficient
C_{zs}	measured static lift coefficient
D	electrical displacement, Coulombs-m^{-2}
E	effective Young's modulus of blade structure, lb-in^{-2}, or electric field intensity, V-m^{-1}
f	equivalent flat plate drag area of fuselage, in^2
G	effective shear modulus of blade structure, lb-in^{-2}
I_β	blade flapping inertia, $\int_0^R mr^2 dr = \frac{1}{3} mR^3$ (uniform blade)
I_θ	blade pitch moment of inertia, $\int_0^R mk_m^{\ 2} dx$
$\bar{k}$	average value of inverse of reduced velocity, b/r
K_β	blade flapping root spring rate, in-lb-rad^{-1}
K_θ	blade pitch root spring rate, in-lb-rad^{-1}
L	number of out-of-plane bending assumed modal functions
L_w	section lift force, lb-in^{-1}
$\bar{L}_w$	nondimensional section lift force, $L_w / m\Omega^2 R$
m	blade mass distribution, lb-sec^2-in^{-1}/in
M	number of torsional assumed modal functions, or section Mach number
M_ϕ	section pitching moment about $c/4$, in-lb/in
$\bar{M}_\phi$	nondimensional section pitching moment, $M_\phi / m\Omega^2 R^2$
N	number of aerodynamic evaluation points along blade; number of rotor blades
R	rotor radius, in
x	blade radial coordinate, in
t	time, sec
T	rotor thrust, lb

u	blade axial elastic deflection, in
$\bar{u}$	normalized blade axial deflection, $\bar{u} \equiv u/R$
U	section normalized velocity, $V/\Omega R$
v	blade in-plane elastic deflection, in
$\bar{v}$	normalized blade in-plane elastic deflection, $\bar{v} \equiv v/R$
V_∞	helicopter forward flight velocity, in sec^{-1}
w	out-of-plane elastic deflection, in
$\bar{w}$	normalized blade in-plane elastic deflection, $\bar{w} \equiv w/R$
$\bar{x}$	nondimensional radial coordinate, x/R
y_{ac}	distance of aerodynamic center forward of pitch axis, in
e	distance of mass center forward of pitch axis, in
α	airfoil section angle of attack, rad
α_s	rotor shaft angle, rad
γ	blade Lock number, $\gamma \equiv \rho acR^4 / I_\beta$
$\bar{\Gamma}$	section nondimensional circulation, $\bar{\Gamma} = \bar{L}_z / U$
$\bar{\Gamma}_1$	linear model (unstalled) component of section nondimensional circulation
$\bar{\Gamma}_2$	component of section nondimensional circulation due to stall
$\bar{\Gamma}_{m2}$	normalized section pitching moment deviation due to stall, $\bar{\Gamma}_{m2} \equiv C_{m2}/U$
Δ_i	normalized width of ith aerodynamic segment
ε	permittivity of piezoelectric material,
$\overset{*}{\varepsilon}$	section rotation rate with respect to the air mass, rad-sec^{-1}
ϕ	torsional deflection, rad
$\bar{x}_i$	normalized midpoint position of ith aerodynamic segment
λ_T	rotor tip-path plane inflow ratio, $\lambda_T = \nu/\Omega R$
μ	rotor advance ratio, $V_\infty/\Omega R$
ν	rotor uniform inflow induced velocity, in sec^{-1}
ρ	air density, lb-sec^2-in^{-1}/in^3
σ	rotor solidity, $\sigma = Nc/\pi R$
θ	section pitch angle, $\theta = \theta_{con} + \phi$, rad
θ_{con}	blade control pitch setting, $\theta_{con} = \theta_0 + \theta_{1c}\cos\psi + \theta_{1s}\sin\psi$, rad
θ_0	blade collective pitch input angle, rad
θ_{1s}	lateral cyclic pitch input, rad
θ_{1c}	longitudinal cyclic pitch input, rad
$\bar{\omega}_\phi$	nondimensional root pitch natural frequency, $\sqrt{K_\phi / I_\theta \Omega^2}$
Ω	rotor rotational speed, rad sec^{-1}
ψ	blade azimuth angle, rad
$\overset{*}{(\,)}$	$d(\,)/d\psi$
$(\,)^+$	$d(\,)/d\bar{x}$

AN AEROELASTIC ANALYSIS OF HELICOPTER ROTOR BLADES INCORPORATING PIEZOELECTRIC FIBER COMPOSITE TWIST ACTUATION

W. Keats Wilkie
NASA Langley Research Center, Hampton, VA 23681

K. C. Park
University of Colorado, Boulder, CO 80309

ABSTRACT

A simple aeroelastic analysis of a helicopter rotor blade incorporating embedded piezoelectric fiber composite, interdigitated electrode blade twist actuators is described. The analysis consists of a linear torsion and flapwise bending model coupled with a nonlinear ONERA based unsteady aerodynamics model. A modified Galerkin procedure is performed upon the rotor blade partial differential equations of motion to develop a system of ordinary differential equations suitable for dynamics simulation using numerical integration. The twist actuation responses for three conceptual full-scale blade designs with realistic constraints on blade mass are numerically evaluated using the analysis. Numerical results indicate that useful amplitudes of nonresonant elastic twist, on the order of one to two degrees, are achievable under one-g hovering flight conditions for interdigitated electrode poling configurations. Twist actuation for the interdigitated electrode blades is also compared with the twist actuation of a conventionally poled piezoelectric fiber composite blade. Elastic twist produced using the interdigitated electrode actuators was found to be four to five times larger than that obtained with the conventionally poled actuators.

1. INTRODUCTION

Significant undesirable fixed system and rotating system vibratory loads continue to exist on all helicopters. These vibratory loads are primarily the result of responses generated by unsteady aerodynamic loads acting on the main rotor system while the helicopter is in forward flight. Since high vibratory loads result in increased maintenance requirements and poor ride quality, much effort has been devoted to finding means to eliminate or reduce them.

Many mechanical devices, mounted either in the fixed system (fuselage), or rotating system (hub, and occasionally blades), have been developed for this purpose.[1, 2] The majority of these mechanisms essentially attempt to alleviate the undesirable vibratory loads by introducing counteracting inertial and damping forces. This approach has the drawback of requiring the addition of mechanisms, with attendant mass and complexity and sometimes performance degradation, to the vehicle. In contrast to these methods, the techniques of higher harmonic control (HHC),[3, 4] and individual blade control (IBC),[5, 6, 7, 8] seek to eliminate vibrations at their aerodynamic source; by directly altering the unsteady aerodynamic forces acting on the rotor blades. This is accomplished by introducing cyclic variations in the root pitch of each blade, either

by clever manipulation of the existing (swashplate) control system, or through the use of auxilliary pitch actuators mounted within the rotating system.

HHC active control through a swashplate-type mechanism is restricted by fundamental rotor dynamics to cyclic pitch inputs at the blade passage frequency ($N\Omega$), and the next higher and lower harmonics of the blade passage frequency ($(N \pm 1)\Omega$), only, where N is the number of rotor blades, and Ω is the rotational speed. HHC can also be limited by the typically low bandwidth characteristics of swashplate hydraulic actuation systems.

The IBC approach, on the other hand, enables individual control of blade pitch at essentially arbitrary frequencies. This is accomplished through auxilliary pitch control actuators placed within the rotating system. With few exceptions, hydraulics based systems have proven to be the best means of providing the power and bandwidth in the rotating system necessary for useful IBC. However, the added complexity associated with delivering hydraulic power from the fixed system to the rotating system has made practical implementation of IBC on production helicopters prohibitive.

1.1 Smart material IBC actuation schemes.

Methods of using smart materials to deflect trailing edge control flaps,[9, 10, 11] or actuate blade twist[12,13] electromechanically have been advanced as a more practical alternative means of implementing some form of IBC. Electrical power for smart material actuators has the advantage of being easily deliverable from the fixed system to the rotating system through conventional slipring devices. This avoids the complications associated with transferring fixed system hydraulic power for individual blade actuators to the rotating system. The bandwidth characteristics of certain smart material actuators are also superior to those of hydraulic and conventional electromechanical, or servomotor, actuators.

Currently, trailing edge flap actuation has the advantage over other smart material IBC schemes in that available smart material power and displacement capabilities are very near those required for a practical rotor blade flap actuator design. Disadvantages of the trailing edge flap include the undesirable addition of complicated mechanisms to the rotor system, and to a lesser extent, the degradation of flap aerodynamic force and moment performance due to hinge lines.

Blade twist actuation is attractive by virtue of being mechanically simple and aerodynamically efficient. However, as rotor blade structures tend to be relatively stiff in torsion, induction of useful levels of twist using smart materials can be difficult. In addition, the added mass of the embedded smart materials can also be prohibitive when developing practical induced twist blade systems. Despite these drawbacks, some encouraging developments in twist actuation of smart material structures continue to be made. Most recently, research in anisotropic twist actuation of plate structures using piezoelectric fiber composites (PFC)[14, 15] has demonstrated that relatively high levels of twist actuation are potentially achievable. The application of interdigitated electrode technology (IDE)[16] can in principle enhance the performance of these materials even further.

1.2 Previous work related to analysis of on-blade active control.

To date, relatively little analytical work has been reported detailing the aeroelastic behavior of rotor blades incorporating either trailing edge control flaps or controllable twist. Millott and Friedman[17] have given the most comprehensive treatment so far with respect to the unsteady aerodynamics of rotor blade trailing edge control flaps, and their employment as vibration reduction devices. Specific methods for actuation of control flaps were not addressed in their work however. Use of control flaps to generate higher harmonic controllable twist was investigated analytically and experimentally in full-scale wind tunnel tests performed in the 1970's. The analytical portions of this investigation were conducted by Lemnios and Dunn,[18] with wind tunnel results reported by Wei and Weisbrich.[19] Significant vibration reductions were reported using flap actuation at 0Ω, 1Ω, 2Ω, 3Ω, and 4Ω frequencies. However, flap actuation was achieved only by use of a relatively complex system of mechanical linkages, which would not be generally suitable for flight test or production vehicles. A related investigation of the performance effects of variable camber was also carried out by Dadone, Cowan, and McHugh.[20] Analytical results suggested that significant improvements in overall rotor performance were achievable, especially when airfoil camber changes were used to induce blade twist. Techniques for affecting camber changes on rotor blades were discussed only in conceptual terms.

Even less has been reported on the analysis of the aeroelastic behavior of rotor blade structures specifically incorporating embedded smart material actuators. Song and Lebrescu[21] developed the equations of motion for a rotating, thin-walled, cantilevered beam structure incorporating embedded piezoelectric actuators. No aerodynamic forcing was included in their study, and actuation of torsional motion was not considered. Nitzsche and Breitbach recently reported the results of a study to evaluate the ability of embedded piezoelectric materials to attenuate out-of-plane bending and torsional vibrations on a rotor blade structure.[22] To accomplish this, they developed a rotor blade aeroelastic model incorporating quasi-static aerodynamics and a "directionally attached piezoelectric crystal" bending-torsion actuation scheme similar to that developed by Barrett. They concluded that the lightly damped torsional blade modes could be significantly affected on a practical blade structure without saturation of the piezoelectric materials.

1.3 Scope of this effort.

For the most part, aeroelastic analysis of rotor blades incorporating on-blade actuation is still very much in its infancy. In particular, there is a lack of simple analytical models suitable for conducting preliminary conceptual control and design studies for embedded smart material blade structures. In light of this, and in order to gain greater insight into the control and aeroelastic response issues related to induced twist smart structure rotor blades, a simple aeroelasticity model for a piezoelectric fiber composite twist actuated helicopter rotor blade has been developed by the authors. This model is derived specifically for use in the investigation of phenomena related to torsional control and response of helicopter rotor blades incorporating piezoelectric twist. In this

paper, a description of the derivation and numerical implementation of this model is given. Additionally, numerical results demonstrating the twist actuation potential of three conceptual full-scale helicopter blade designs are shown. The work reported here is thought to be the first specifically related to the aeroelastic analysis of piezoelectric fiber composite twist actuated helicopter rotor blades.

2. ANALYTICAL MODEL DESCRIPTION

A rotor blade aeroelasticity model may be thought of as a unification of several basic analytical submodels. These submodels are, at a minimum, 1) a formulation of the blade structural dynamics, including all forces related to blade rotation, 2) a formulation of the aerodynamic forces and moments acting on the blade, 3) an inflow model, and 4) a control formulation. These submodels may be coupled in many ways depending on the degree of complexity of the overall formulation. In this development, they will be conceptually linked as shown in Figure 1. Theoretical descriptions of each submodel are given below.

2.1 Structural formulation

The equations of motion used here to describe the elastic torsion and out-of-plane bending behavior of an isolated helicopter rotor blade are adapted from the general elastic bending and torsion deformation equations developed by Kaza and Kvaternik.[23] Due to the complexity of these equations, and elastic rotor blade equations of motion in general, it is usually necessary to apply some simplifying assumptions to the complete set of equations in order to obtain a more mathematically manageable model. An ordering scheme approach is used here to accomplish this. Use of such a procedure enables one to avoid a great deal of the complicated algebra associated with retention of "high order" nonlinear terms in the equations, and ensures that the most physically significant terms are retained.

The first step in employing an ordering scheme is to rewrite the equations of motion in a nondimensional form. An order is then assigned to each nondimensional term in the equations relative to an assumed scale factor, ε , and the equations are rewritten retaining only terms of the lowest order, and terms of one order greater. Terms of two orders greater and higher are usually discarded. For this study ε will be assigned a value of 0.10, which is equal to the assumed order of magnitude of torsional deformations, hence, $O(0)=1$, $O(\varepsilon)=0.10$, $O(\varepsilon^2)=0.01$, etc.

Evaluation of the order of each nondimensional term is based on the intended application of the final equations, e.g., stability, vibration, etc., and representative full-scale helicopter structural and flight parameters. The ordering of parameters used in this study is based on schemes applicable to rotorcraft vibrations, and is shown in Table 1.

Three additional assumptions related to the blade geometry are also made. These are, 1) that the blade precone angle and built in twist are assumed to be zero, 2) the blade structural cross-section

is assumed to be doubly symmetric, and 3) the blade pitch radius of gyration is assumed to be approximately equal to the k_{m2} cross section integral (i.e., $k_{m1}/k_{m2}<<1$).

Applying the ordering scheme, with the additional assumptions given above, to the equations of Reference 23 yields the following partial differential equations of motion for blade out-of-plane bending and torsion. (Blade coordinates are illustrated in Figure A1.)

Out-of-plane (flapwise) bending ($O(\varepsilon)$, $O(\varepsilon^4)$):

$$\ddot{\overline{w}} - \left(\frac{T}{m\Omega^2 R^2} \overline{w}^{+} \right)^{+} + \underline{\overline{e}\left(\ddot{\phi} + \ddot{\theta} \right) - \left\{ \overline{e}\overline{x}\left(\theta + \phi \right) \right\}^{+}} + \underline{\underline{\left\{ \frac{EI_{\eta\eta}}{m\Omega^2 R^4} \overline{w}^{++} \right\}^{++} + \left\{ \frac{E^* I_{\eta\eta}}{m\Omega R^3} \dot{\overline{w}}^{++} \right\}^{++}}} = \frac{L_w}{m\Omega^2 R^2} \tag{1}$$

Torsional deformation ($O(\varepsilon^4,\varepsilon^5)$):

$$\frac{k_m^{\,2}}{R^2}\left(\ddot{\phi} + \ddot{\theta} \right) + \frac{k_m^{\,2}}{R^2}\phi - \left[\frac{T}{m\Omega^2 R^2} \frac{k_A^{\,2}}{R^2} \phi^{+} \right]^{+} + \overline{e}\left[\overline{x}\overline{w}^{+} + \ddot{\overline{w}} \right]$$
$$- \left(\frac{GJ}{m\Omega^2 R^4} \phi^{+} \right)^{+} - \left(\frac{G^* J}{m\Omega R^4} \dot{\phi}^{+} \right)^{+} = \frac{M_\phi}{m\Omega^2 R^2} - \frac{Q_{PE}^{\;+}}{m\Omega^2 R^2} - \frac{k_m^{\,2}}{R^2}\theta \tag{2}$$

The blade section tension force, T, is based on an $O(1)$ approximation, and is given by

$$T \cong \Omega^2 R^2 \int_{\overline{x}}^{1} m\overline{x} d\overline{x} \,. \tag{3}$$

Temporal differentiations (denoted by *) in the above equations are performed with respect to the rotor azimuth, ψ, which, for constant rotational velocity Ω, is $\psi \equiv \Omega t$. Spatial differentiations (denoted by $^{+}$) are conducted with respect to the nondimensional blade radial location, $\overline{x} \equiv x/R$. Descriptions of the coordinate systems used to describe the blade motions may be found in Appendix A.

Note that the single underlined terms in Equation 1 are actually of $O(\varepsilon^4)$, but are retained in order to ensure mathematical symmetry in the resulting mass and stiffness matrices. Double underlined terms in Equation 1 are also of $O(\varepsilon^4)$, but are kept so that the equation is a more physically meaningful representation of out-of-plane bending. Technically, retention of all $O(\varepsilon^4)$ terms would require inclusion of additional terms associated with the in-plane ("lead-lag") bending deformation of the blade; terms that have been consistently ignored in this treatment. A higher

order approximation of the tension force would be also be necessary for consistency. We re-emphasize that these equations were developed primarily for use in investigations related to blade torsional response and control. Consequently, studies of out-of-plane vibratory response using the present formulation should be done with some degree of caution.

Q_{PE} , in Equation 2, represents the piezoelectric induced twisting moment, which will be derived in the control formulation section below.

A modified Galerkin procedure[24] is used here to obtain modal solutions to Equations 1-3. In this case, superposition solutions for w and ϕ of the form,

$$\overline{w}(\overline{x},\psi) = \sum_{l=1}^{L} \overline{w}_l(\psi) W_l(\overline{x}), \tag{4}$$

$$\phi(\overline{x},\psi) = \sum_{m=1}^{M} \phi_m(\psi) \Phi_m(\overline{x}), \tag{5}$$

are assumed, where L and M are the number of out-of-plane bending and torsional modal functions respectively. In the modified Galerkin procedure, these modal functions need only satisfy the geometric boundary conditions on the blade. Work due to any nonfulfilled "natural" boundary conditions is accounted for with additional boundary terms in the equations. Substituting Equations 4 and 5 into Equation 1, and performing the appropriate integrations, yields a set of L ordinary differential equations of the following form:

$$\begin{aligned}
&\sum_{l=1}^{L} \overset{**}{\overline{w}}_l \int_0^1 W_l W_n \, d\overline{x} \\
&+ \sum_{l=1}^{L} \overset{*}{\overline{w}}_l \int_0^1 \frac{E^* I_{\eta\eta}}{m\Omega^2 R^3} W_l^{++} W_n^{++} \, d\overline{x} \\
&+ \sum_{l=1}^{L} \overline{w}_l \left(\int_0^1 \frac{T}{m\Omega^2 R^2} W_l^{+} W_n^{+} \, d\overline{x} + \int_0^1 \frac{EI_{\eta\eta}}{m\Omega^2 R^4} W_l^{++} W_n^{++} \, d\overline{x} + \frac{K_\beta}{\Omega^2 R^2 \int_0^1 m \, d\overline{x}} W_l^{+}(0) W_n^{+}(0) \right), \\
&+ \sum_{m=1}^{M} \overset{**}{\phi}_m \int_0^1 \overline{e} \Phi_m W_n \, d\overline{x} + \sum_{m=1}^{M} \phi_m \int_0^1 \overline{e}\overline{x} \Phi_m W_n^{+} \, d\overline{x} \\
&= \int_0^1 \frac{L_w}{m\Omega^2 R} W_n \, d\overline{x} - \left(\overset{**}{\theta} \int_0^1 \overline{e} W_n \, d\overline{x} + \theta \int_0^1 \overline{e}\overline{x} W_n^{+} \, d\overline{x} \right)
\end{aligned} \tag{6}$$

where $n = 1, L$. A similar procedure performed on Equation 2 yields an additional set of M ordinary differential equations;

$$
\begin{aligned}
&\sum_{m=1}^{M} \overset{**}{\phi}_m \int_0^1 \frac{k_m{}^2}{R^2} \Phi_m \Phi_p d\bar{x} \\
&\sum_{m=1}^{M} \overset{*}{\phi}_m \int_0^1 \frac{G^* J}{m\Omega^2 R^3} \Phi_m^+ \Phi_p^+ d\bar{x} \\
&+\sum_{m=1}^{M} \phi_m \left(\int_0^1 \frac{k_m{}^2}{R^2} \Phi_m \Phi_p d\bar{x} + \int_0^1 \frac{T}{m\Omega^2 R^2} \frac{k_A{}^2}{R^2} \Phi_m^+ \Phi_p^+ d\bar{x} + \int_0^1 \frac{GJ}{m\Omega^2 R^4} \Phi_m^+ \Phi_p^+ d\bar{x} + \frac{K_\theta}{\Omega^2 R^2 \int_0^1 m d\bar{x}} \Phi_m(0) \Phi_p(0) \right), \\
&+\sum_{l=1}^{L} \overset{**}{\bar{w}}_l \int_0^1 \bar{e} W_l \Phi_p d\bar{x} + \sum_{l=1}^{L} \bar{w}_l \int_0^1 \bar{e}\bar{x} W_l^+ \Phi_p d\bar{x} \\
&= \int_0^1 \frac{M_\phi}{m\Omega^2 R^2} \Phi_p d\bar{x} + \int_0^1 \frac{Q_{PE}}{m\Omega^2 R^2} \Phi_p^+ d\bar{x} - \left(\overset{**}{\theta} + \theta \right) \int_0^1 \frac{k_m{}^2}{R^2} \Phi_p dx
\end{aligned}
\tag{7}
$$

with $p = 1, M$.

The K_β and K_θ terms in Equations 6 and 7, which do not appear in Equations 3 and 4, are used to represent finite stiffnesses present at $\bar{x} = 0$. These terms can be used to account for the stiffness of a mechanical flapping spring placed at the blade root, or the inherent flexibility of the pitch control system.

It should be noted that all stiffness, damping, and inertia terms contained in the above equations represent the structural properties of the combined piezoelectric/passive material blade structure. The derivation of the stiffness terms is contained in Appendix B.

2.2 Aerodynamic formulation

The sectional lifting forces and moments are calculated using a technique based on the ONERA dynamic stall model developed by Tran and Petot.[25] The ONERA model uses differential equations in time to describe the unsteady aerodynamic lifting forces and pitching moments, including dynamic stall effects, acting upon an airfoil section undergoing arbitrary pitch and plunge motion.

2.2.1 Section lift formulation

Modifications to the ONERA model for general use in rotorcraft aerodynamic formulations have been made by Peters,[26] with nondimensional circulations used as the state variables instead of aerodynamic coefficients. The simplified lift circulation equations of Reference 26, which are well behaved in the reverse flow region of the rotor disk, but do not give lift reversal, are used here (8, 9).

$$\bar{L}_Y = \bar{L}_0 + U_X\left(\bar{\Gamma}_1 + \bar{\Gamma}_2\right) \tag{8a}$$

$$\bar{L}_X = -U_Y\left(\bar{\Gamma}_1 + \bar{\Gamma}_2\right) \tag{8b}$$

$$\bar{L}_0 = \bar{b}\, s_z \overset{*}{U}_Y \tag{8c}$$

$$\bar{k}\,\overset{*}{\bar{\Gamma}}_1 + \lambda_z \bar{\Gamma} = \lambda_z a U_Y + \delta_z \bar{b}\,\overset{*}{\varepsilon} \tag{9a}$$

$$\begin{aligned} &\bar{k}^2\,\overset{**}{\bar{\Gamma}}_2 + 2 d_z w_z \bar{k}\,\overset{*}{\bar{\Gamma}}_2 + w_z^{\,2}\left(1 + d_z^{\,2}\right)\bar{\Gamma}_2 \\ &= -w_z^{\,2}\left(1 + d_z^{\,2}\right)\left[U_X \Delta C_z + e_z \bar{k}\left(\overset{*}{U}_X\, \Delta C_z + \frac{\partial \Delta C_z}{\partial \alpha}\overset{*}{U}_Y\right)\right] \end{aligned} \tag{9b}$$

$\bar{L}_0$ in equation (8c) is the nondimensional apparent mass lift. $\bar{L}_X$ and $\bar{L}_Y$ are the components of the nondimensional lift in the airfoil section X and Y directions respectively. The nondimensional section velocities U, U_Y, and U_Z, and section angle of attack, α, are derived in Appendix C. $\overset{*}{\varepsilon}$ in equations (9) is defined as the geometric rate of rotation of the airfoil with respect to the air mass (see Appendix C), and is given here by

$$\overset{*}{\varepsilon} \equiv \frac{d\varepsilon}{d\psi} \cong \overset{*}{\theta}_{con} + \overset{*}{\phi} + \overset{*}{\bar{w}}^{+}. \tag{10}$$

ΔC_z in Equations 9 is the difference between the linear model static lift coefficient, C_{zl} and the measured stalled lift coefficient, C_{zs}, i.e.,

$$\Delta C_z = C_{zl} - C_{zs}\,.$$

Plots of the static lift coefficient data used in this model are shown in Figure 2. These curves are extrapolated from curves given in References 28 and 29.

The angle of attack dependent coefficients (s, λ, δ, d, w, and e) are derived from experimental two-dimensional unsteady airfoil tests using the parameter identification scheme described in Reference 25. Parameter values for the ONERA OA212 rotorcraft airfoil are used in this model, and are shown in Table 2.

2.2.2 Section Pitching Moment Formulation

Improvements to the basic ONERA pitching moment formulation have been made by Petot,[27] with further modifications made by Chouchane[28] (given also by Peters, Chouchane, and Fulton[29]), and this is the representation used in this model. In this approach, the unstalled component of C_m is given explicitly through the static moment coefficient, which is a function of angle-of-attack only. This results in the elimination of one state per spanwise aerodynamic evaluation point in the model. Plots of the static pitching moment data used here are shown in Figure 3. These curves are extrapolated from curves given in References 28 and 29, and from data provided by Tang.[30]

The stalled contribution to the section pitching moment is calculated using a circulation based model similar to that developed for section lift. The second order differential equation describing this stalled pitching moment circulation, defined as $\overline{\Gamma}_{m2} \equiv UC_{m2}$, is shown below (11).

$$\bar{k}_i^{\,2}\,\overset{**}{\overline{\Gamma}}_{m2i} + a_{m_i}\bar{k}_i\,\overset{*}{\overline{\Gamma}}_{m2i} + r_{m_i}\overline{\Gamma}_{m2i} = -r_{m_i}U_i\Delta C_{m_i} - E_{m_i}\bar{k}_i\,\overset{*}{U}_{y_i} \tag{11}$$

The coefficients a_m, r_m, and E_m in Equation 11 were found by Petot (Reference 27) to have similar characteristics for many airfoils. Expressions for these coefficients, omitting subscripts, may be written as

$$a_m = a_0 + a_2\Delta C_z^{\,2}, \tag{12a}$$

$$r_m = \left(r_0 + r_2\Delta C_z^{\,2}\right)^2, \tag{12b}$$

$$E_m = E_2\Delta C_z^{\,2}. \tag{12c}$$

Values of a_0, a_2, r_0, r_2, and E_2 used in the present formulation are taken from the generic "mean airfoil" values of Reference 27, and are provided in Table 3.

2.2.3 Airloads calculation

The aerodynamic forcing integrals present in Equations 6 and 7 are calculated by first evaluating the sectional aerodynamic forces and moments per unit length at N discrete points along the blade span. Section aerodynamic forces and moments are further assumed to be constant over the width of each section. Consistent with the ordering scheme assumed in the structural formulation above, the final expressions for these aerodynamic loading integrals are

$$\int_0^1 \bar{L}_w W_l\,d\bar{x} = \frac{\gamma}{6a}\sum_{i=1}^{N}\left[U_i\left(\overline{\Gamma}_{1_i} + \overline{\Gamma}_{2_i}\right) + \bar{L}_{0_i}\right]\int_{\bar{r}_i}^{\bar{r}_{i+1}} W_l\,d\bar{x}, \tag{13}$$

$$\int_0^1 \overline{M}_\phi \Phi_m d\bar{x} =$$

$$\frac{\gamma \bar{c}}{6a} \sum_{i=1}^{N} \left\{ U_i^2 C_{m\ell_i} + U_i \overline{\Gamma}_{m2_i} + c_1 \bar{b}\, \overset{*}{U}_{y_i} + c_2 U_i \overset{*}{\varepsilon} \Big|_{\bar{x}_i} + c_3 \bar{b}^2 \left(\overset{**}{\theta} + \overset{**}{\phi} \right) \Big|_{\bar{x}_i} + \bar{y}_{ac} \left[U_i \left(\overline{\Gamma}_{1_i} + \overline{\Gamma}_{2_i} \right) + \overline{L}_{0_i} \right] \right\} \int_{\bar{r}_i}^{\bar{r}_{i+1}} \Phi_m d\bar{x} \tag{14}$$

$\bar{r}_i$, in Equations 13 and 14, is the radial location of the inboard edge of the ith aerodynamic section,

$$\bar{r}_i = \bar{x}_i - \Delta_i / 2 ,$$

where $\bar{x}_i$ is the nondimensional radial location of the ith aerodynamic evaluation point, and Δ_i the associated nondimensional section width.

2.3 Inflow model

A uniform rotor inflow model, based on momentum theory (e.g., Gessow and Myers[31]), is used in this formulation. A uniform inflow assumption, i.e., the assumption of constant inflow velocity at every location across the rotor disk, is not unreasonable for hovering or vertical flight conditions, although it is not very realistic for forward flight. Nevertheless, it is used here for computational simplicity in the numerical model. More complex inflow representations will be incorporated into future versions of this analysis.

For an implicitly trimmed rotor operating at thrust coefficient C_T, and forward flight advance ratio μ, the uniform induced velocity ratio with respect to the tip-path-plane may be written as

$$\lambda_{TPP} = \mu \tan \alpha_s + \lambda_i , \tag{15}$$

where

$$\lambda_i = \frac{C_T}{2\sqrt{\mu^2 + \lambda_{TPP}{}^2}} . \tag{16}$$

An Newton-Raphson iterative approach, from Johnson[32] is used to numerically evaluate λ_{TPP} in the above expression, i.e. (17)

$$\left(\lambda_{TPP}\right)_{n+1} = \left(\frac{\mu \tan\alpha_s + \frac{C_T}{2} \frac{\left(\mu^2 + 2\lambda_{TPP}{}^2\right)}{\left(\mu^2 + \lambda_{TPP}{}^2\right)^{3/2}}}{1 + \frac{C_T}{2} \frac{\lambda_{TPP}}{\left(\mu^2 + \lambda_{TPP}{}^2\right)^{3/2}}} \right)_n . \tag{17}$$

Usually only two or three iterations are required for the calculation to converge, starting with

$$\lambda_{TPP} = \mu \tan\alpha_s + \frac{C_T}{2\sqrt{\mu^2 + C_T/2}} . \tag{18}$$

2.4 Control formulation

2.4.1 Trim control

Swashplate control angles are calculated using trim equations adapted from the harmonic balance equations of Reference 32. These equations, rewritten assuming zero blade twist and no first harmonic flapping with respect to the rotor shaft, are given by

$$\theta_0 = \frac{\left(1 + \frac{3}{2}\mu^2\right)\left(\frac{6C_T}{\sigma a}\right) + \frac{3}{2}\lambda_{TPP}\left(1 - \frac{1}{2}\mu^2\right)}{1 - \mu^2 + \frac{9}{4}\mu^4}, \tag{19a}$$

$$\theta_{1s} = -\frac{\frac{8}{3}\mu\left(\frac{6C_T}{\sigma a}\right) + 2\mu\lambda_{TPP}\left(1 - \frac{3}{2}\mu^2\right)}{1 - \mu^2 + \frac{9}{4}\mu^4}, \tag{19b}$$

$$\theta_{1c} = \frac{\frac{4}{3}\mu\beta_0}{1 + \frac{1}{2}\mu^2}, \tag{19c}$$

where β_0 in equation 19c is the estimated blade coning angle given by

$$\beta_0 = \frac{\frac{\gamma}{8}}{1-\mu^2+\frac{9}{4}\mu^4}\left[\left(1-\frac{19}{18}\mu^2+\frac{3}{2}\mu^4\right)\frac{6C_T}{\sigma a}+\left(\frac{1}{6}-\frac{7}{12}\mu^2+\frac{1}{4}\mu^4\right)\lambda_{TPP}\right].$$

(19d)

The control settings predicted using these trim equations are reasonably effective at eliminating first harmonic flapping in unstalled flight. However, under heavily stalled forward flight conditions, these equations will fail to trim the rotor effectively.

2.4.2 Piezoelectric twisting moment

The piezoelectric actuator equation development detailed here borrows heavily from the approach used by Bent, Hagood, and Rogers.[15] Their equations, however, have been rewritten here explicitly for the case of in-plane polarization of the piezoelectric lamina material, or interdigitated electrode (IDE) poling.[16] Such an IDE configuration, in principal, allows the so-called "d_{33} effect" to be used to maximum advantage to enhance the inplane strain actuation capabilities of the piezoelectric lamina. This in turn should result in an increase in torsional actuation capability of the lamina with respect to conventionally poled schemes.

Development of the actuator equations begins with an alternate version of the standard linear piezoelectric constitutive relations.[33] Assuming structural orthotropy in the piezoelectric material, and applying the plane stress assumption ($T_3=T_4=T_5=0$) to the constitutive relations yields

$$\begin{Bmatrix} D_1 \\ D_2 \\ D_3 \\ S_1 \\ S_2 \\ S_6 \end{Bmatrix} = \begin{bmatrix} \varepsilon_{11}^T & 0 & 0 & d_{33} & d_{31} & 0 \\ 0 & \varepsilon_{22}^T & 0 & 0 & 0 & d_{15} \\ 0 & 0 & \varepsilon_{33}^T & 0 & 0 & 0 \\ d_{33} & 0 & 0 & s_{11}^E & s_{12}^E & 0 \\ d_{31} & 0 & 0 & s_{12}^E & s_{22}^E & 0 \\ 0 & d_{15} & 0 & 0 & 0 & s_{66}^E \end{bmatrix} \begin{Bmatrix} E_1 \\ E_2 \\ E_3 \\ T_1 \\ T_2 \\ T_6 \end{Bmatrix}.$$

(20)

The S_3, S_4, and S_5 strains, although not necessarily zero, will be neglected here.

The poling direction of the piezoelectric material will be defined to be in the material 1-axis direction (see Figure 4), rather than in the more familiar out-of-plane direction (3-axis). The usual indexing nomenclature in the piezoelectric free-strain coupling coefficients will be retained here however. This is solely to allow the d_{33}, and d_{13}, piezoelectric material coefficients to be more readily identified in the resulting equations. (Note that the conventionally poled case may easily be obtained from these equations by setting d_{33} equal to d_{31}.)

Rewriting Equation 20 with strains (S) as independent variables:

$$\begin{Bmatrix} D_1 \\ D_2 \\ D_3 \\ T_1 \\ T_2 \\ T_6 \end{Bmatrix} = \begin{bmatrix} \varepsilon_{11}^S & 0 & 0 & e_{33} & e_{31} & 0 \\ 0 & \varepsilon_{22}^S & 0 & 0 & 0 & e_{15} \\ 0 & 0 & \varepsilon_{33}^S & 0 & 0 & 0 \\ -e_{33} & 0 & 0 & c_{11}^E & c_{12}^E & 0 \\ -e_{31} & 0 & 0 & c_{12}^E & c_{22}^E & 0 \\ 0 & -e_{15} & 0 & 0 & 0 & c_{66}^E \end{bmatrix} \begin{Bmatrix} E_1 \\ E_2 \\ E_3 \\ S_1 \\ S_2 \\ S_6 \end{Bmatrix}, \tag{21}$$

or more compactly,

$$\begin{Bmatrix} \mathbf{D} \\ \mathbf{T} \end{Bmatrix} = \begin{bmatrix} \varepsilon^S & \mathbf{e} \\ -\mathbf{e}^T & \mathbf{c}^E \end{bmatrix} \begin{Bmatrix} \mathbf{E} \\ \mathbf{S} \end{Bmatrix}, \tag{22}$$

where

$$\mathbf{c}^E = \left(\mathbf{s}^E\right)^{-1} \quad \mathbf{e} = \mathbf{d}\mathbf{c}^E \quad \varepsilon^S = \varepsilon^T - \mathbf{d}\mathbf{c}^E(\mathbf{d})^T \ . \tag{23}$$

The relationships between field components given in the global, or beam coordinate system, and those in a system rotated by an angle θ about the 3 direction (actuator system) are given by (see Figure 5)

$$\tilde{\mathbf{D}} = \mathbf{R}_E\mathbf{D} \quad \tilde{\mathbf{E}} = \mathbf{R}_E\mathbf{E} \quad \tilde{\mathbf{S}} = \mathbf{R}_S\mathbf{S} \quad \tilde{\mathbf{T}} = \left(\mathbf{R}_S{}^T\right)^{-1}\mathbf{T}, \tag{24}$$

where

$$\mathbf{D} \equiv \begin{Bmatrix} D_1 \\ D_2 \\ D_3 \end{Bmatrix} \quad \mathbf{E} \equiv \begin{Bmatrix} E_1 \\ E_2 \\ E_3 \end{Bmatrix} \quad \mathbf{S} \equiv \begin{Bmatrix} S_1 \\ S_2 \\ S_6 \end{Bmatrix} \quad \mathbf{T} \equiv \begin{Bmatrix} T_1 \\ T_2 \\ T_6 \end{Bmatrix} \tag{25}$$

(similarly for $\tilde{\mathbf{D}}$, $\tilde{\mathbf{E}}$, $\tilde{\mathbf{S}}$, and $\tilde{\mathbf{T}}$).

The appropriate transformation matrices for this coordinate rotation are

$$\mathbf{R}_s = \begin{bmatrix} \cos^2\theta & \sin^2\theta & \cos\theta\sin\theta \\ \sin^2\theta & \cos^2\theta & -\cos\theta\sin\theta \\ -2\cos\theta\sin\theta & 2\cos\theta\sin\theta & \cos^2\theta - \sin^2\theta \end{bmatrix}, \tag{26}$$

$$\mathbf{R}_E = \begin{bmatrix} \cos\theta & \sin\theta & 0 \\ -\sin\theta & \cos\theta & 0 \\ 0 & 0 & 1 \end{bmatrix}. \tag{27}$$

In terms of the actuator coordinate system, Equation 22 then becomes

$$\begin{Bmatrix} \tilde{\mathbf{D}} \\ \tilde{\mathbf{T}} \end{Bmatrix} = \begin{bmatrix} \tilde{\varepsilon}^S & \tilde{\mathbf{e}} \\ -\tilde{\mathbf{e}}^T & \tilde{\mathbf{c}}^E \end{bmatrix} \begin{Bmatrix} \tilde{\mathbf{E}} \\ \tilde{\mathbf{S}} \end{Bmatrix}. \tag{28}$$

Substituting Equations 24 into Equation 28 yields constitutive relations expressed in terms of the global field variables.

$$\begin{Bmatrix} \mathbf{D} \\ \mathbf{T} \end{Bmatrix} = \begin{bmatrix} \mathbf{R}_E{}^T \tilde{\varepsilon}^S \mathbf{R}_E & \mathbf{R}_E{}^T \tilde{\mathbf{e}} \mathbf{R}_S \\ -\mathbf{R}_S{}^T \tilde{\mathbf{e}}^T \mathbf{R}_E & \mathbf{R}_S{}^T \tilde{\mathbf{c}}^E \mathbf{R}_S \end{bmatrix} \begin{Bmatrix} \mathbf{E} \\ \mathbf{S} \end{Bmatrix} \tag{29}$$

For convenience, electric fields and displacements will be defined as being specified along the actuator system 1-direction only. The electric field within the piezoelectric material will also be assumed to be an average of the field strength between alternating electrodes. (See Reference 16 for a complete description and discussion of the actual electric field distributions produced using IDE schemes.) Equation 29 is then

$$\begin{Bmatrix} \tilde{D}_1 \\ \mathbf{T} \end{Bmatrix} = \begin{bmatrix} \tilde{\varepsilon}_{11}^S & \tilde{\mathbf{e}} \mathbf{R}_S \\ -\mathbf{R}_S{}^T \tilde{\mathbf{e}}^T & \mathbf{R}_S{}^T \tilde{\mathbf{c}}^E \mathbf{R}_S \end{bmatrix} \begin{Bmatrix} \tilde{E}_1 \\ \mathbf{S} \end{Bmatrix}. \tag{30}$$

A material orientation angle that maximizes the actuator induced shear stress is desired here. This will occur for orientation angles of $\theta = \pm 45°$. For the case of $\theta = +45°$, the rotated material matrix of Equation 30 becomes

$$\begin{bmatrix} \tilde{\varepsilon}_{11}^{S} & \tilde{\mathbf{e}}\mathbf{R}_S \\ -\mathbf{R}_S{}^T\tilde{\mathbf{e}}^T & \mathbf{R}_S{}^T\tilde{\mathbf{c}}^E\mathbf{R}_S \end{bmatrix} =$$

$$\begin{bmatrix} \tilde{\varepsilon}_{11}^{S} & \frac{1}{2}\left(\tilde{e}_{33}+\tilde{e}_{31}\right) & \frac{1}{2}\left(\tilde{e}_{33}+\tilde{e}_{31}\right) & \frac{1}{2}\left(\tilde{e}_{33}-\tilde{e}_{31}\right) \\ -\frac{1}{2}\left(\tilde{e}_{33}+\tilde{e}_{31}\right) & \frac{1}{4}\left(\tilde{c}_{11}^{E}+2\tilde{c}_{12}^{E}+\tilde{c}_{22}^{E}\right)+\tilde{c}_{66}^{E} & \frac{1}{4}\left(\tilde{c}_{11}^{E}+2\tilde{c}_{12}^{E}+\tilde{c}_{22}^{E}\right)-\tilde{c}_{66}^{E} & \frac{1}{4}\left(\tilde{c}_{11}^{E}-\tilde{c}_{22}^{E}\right) \\ -\frac{1}{2}\left(\tilde{e}_{33}+\tilde{e}_{31}\right) & \frac{1}{4}\left(\tilde{c}_{11}^{E}+2\tilde{c}_{12}^{E}+\tilde{c}_{22}^{E}\right)-\tilde{c}_{66}^{E} & \frac{1}{4}\left(\tilde{c}_{11}^{E}+2\tilde{c}_{12}^{E}+\tilde{c}_{22}^{E}\right)+\tilde{c}_{66}^{E} & \frac{1}{4}\left(\tilde{c}_{11}^{E}-\tilde{c}_{22}^{E}\right) \\ -\frac{1}{2}\left(\tilde{e}_{33}-\tilde{e}_{31}\right) & \frac{1}{4}\left(\tilde{c}_{11}^{E}-\tilde{c}_{22}^{E}\right) & \frac{1}{4}\left(\tilde{c}_{11}^{E}-\tilde{c}_{22}^{E}\right) & \frac{1}{4}\left(\tilde{c}_{11}^{E}-2\tilde{c}_{12}^{E}+\tilde{c}_{22}^{E}\right) \end{bmatrix}.$$

(31)

Extracting the torsional terms yields

$$\begin{Bmatrix} \tilde{D}_1 \\ T_6 \end{Bmatrix} = \begin{bmatrix} \tilde{\varepsilon}_{11}^{S} & \frac{1}{2}\left(\tilde{e}_{33}-\tilde{e}_{31}\right) \\ -\frac{1}{2}\left(\tilde{e}_{33}-\tilde{e}_{31}\right) & \frac{1}{4}\left(\tilde{c}_{11}^{E}-2\tilde{c}_{12}^{E}+\tilde{c}_{22}^{E}\right) \end{bmatrix} \begin{Bmatrix} \tilde{E}_1 \\ S_6 \end{Bmatrix}.$$

(32)

At this point , for simplicity, we will assume that the structurally effective portion of the blade is a closed, rectangular, thin-walled section (Figure 6). Following a mechanics of materials approach, the piezoelectric induced shear flow, q_{PE}, , for such a structure may be written as

$$q_{PE} = T_6 t_{PE}\,.$$

(33)

where t_{PE} is the piezoelectric lamina thickness. The total piezoelectric torsional moment may then be expressed as

$$Q_{PE} = \oint r q_{PE}\, ds = 2hw q_{PE} = -2A_e\, \tfrac{1}{2}\left(\tilde{e}_{33}-\tilde{e}_{31}\right)\tilde{E}_1 t_{PE}\,.$$

(34)

where h and w are the height and width of the rectangular cross-section, and A_e is the area enclosed by the wall centerline.

Converting to standard piezoelectric coefficients, via Equation 33, yields

$$Q_{PE} = -A_e\left(d_{33}\left(\tilde{c}_{11}^{E}-\tilde{c}_{12}^{E}\right)+d_{31}\left(\tilde{c}_{12}^{E}-\tilde{c}_{22}^{E}\right)\right)\tilde{E}_1 t_{PE}\,.$$

(35)

For further convenience, we will rewrite Equation 35 in terms of the assumed maximum produceable piezoelectric strain, Λ_{max}, yielding

$$Q_{PE} = -A_e \tilde{c}_{11}^E \left(\left(1 - \frac{\tilde{c}_{12}^E}{\tilde{c}_{11}^E} \right) + \frac{d_{31}}{d_{33}} \left(\frac{\tilde{c}_{12}^E}{\tilde{c}_{11}^E} - \frac{\tilde{c}_{22}^E}{\tilde{c}_{11}^E} \right) \right) \Lambda_{\max} t_{PE} \frac{\tilde{E}_1}{\tilde{E}_{1\max}} \tag{36}$$

where $\Lambda_{\max} \equiv d_{33} \tilde{E}_{1\max}$.

Substituting Equation 36 into the expression for the generalized nondimensional piezoelectric control moments, from Equation 7, yields

$$\int_0^1 \frac{Q_{PE}}{m\Omega^2 R^2} \Phi_m^+ d\bar{x} = -\int_0^1 \frac{A_e \tilde{c}_{11}^E}{m\Omega^2 R^3} \left(\left(1 - \frac{\tilde{c}_{12}^E}{\tilde{c}_{11}^E} \right) + \frac{d_{31}}{d_{33}} \left(\frac{\tilde{c}_{12}^E}{\tilde{c}_{11}^E} - \frac{\tilde{c}_{22}^E}{\tilde{c}_{11}^E} \right) \right) \Lambda_{\max} t_{PE} \frac{\tilde{E}_1}{\tilde{E}_{1\max}} \Phi_m^+ d\bar{x} . \tag{37}$$

If the electrode layers are divided into P independently energizable sections, the average electric field intensity within the pth section is given by

$$\tilde{E}_{1p}(\psi, \bar{x}) = \tilde{E}_{1\max} e_p(\psi), \qquad \bar{r}_p < \bar{x} < \bar{r}_{p+1} \tag{38}$$

where e_p is the electric field generalized field strength, $\bar{r}_p$ is the radial location of the inboard edge of the pth electrode segment, and $\tilde{E}_{1\max}$ is the maximum electrical field permissable without depolarization of the piezoelectric material.

Substituting Equation 37 into 38 yields the generalized piezoelectric control moments in their final form

$$\int_0^1 \frac{Q_{PE}}{m\Omega^2 R^2} \Phi_m^+ d\bar{x} = -\sum_{p=1}^{P} e_p \int_{\bar{r}_p}^{\bar{r}_{p+1}} \frac{A_e \tilde{c}_{11}^E}{m\Omega^2 R^3} \left(\left(1 - \frac{\tilde{c}_{12}^E}{\tilde{c}_{11}^E} \right) + \frac{d_{31}}{d_{33}} \left(\frac{\tilde{c}_{12}^E}{\tilde{c}_{11}^E} - \frac{\tilde{c}_{22}^E}{\tilde{c}_{11}^E} \right) \right) \Lambda_{\max} t_{PE} \Phi_m^+ d\bar{x} . \tag{39}$$

Material properties appearing in Equation 39 for the piezoelectric laminae used in the numerical portion of this study are given in Table 4.

3. NUMERICAL IMPLEMENTATION

The equations of motion for the structural and aerodynamic degrees of freedom are rewritten in state variable form for numerical integration. The structural state derivatives thus will be of the following form:

$$\overset{*}{\mathbf{q}}_{struct} = \begin{bmatrix} -M^{-1}C & -M^{-1}K \\ I & 0 \end{bmatrix} \mathbf{q}_{struct} + \begin{Bmatrix} M^{-1}\left\{ \bar{\mathbf{f}}_{aero} + \bar{\mathbf{f}}_{PE} + \bar{\mathbf{f}}_{\theta_0} \right\} \\ 0 \end{Bmatrix}, \tag{40}$$

with the structural state vector defined as

$$\mathbf{q}_{struct} \equiv \begin{Bmatrix} \overset{*}{\mathbf{x}} \\ \mathbf{x} \end{Bmatrix}. \tag{41}$$

The definitions of *M*, *C*, *K*, etc., may be found in Appendix D. For each aerodynamic evaluation point along the blade, three state variables are required to define the lifting force and two to define the pitching moment. The aerodynamic state derivatives for each such point are

$$\overset{*}{\mathbf{q}}_{aero\,i} = \begin{Bmatrix} f_{1i}\overline{\Gamma}_{1i} + f_{2i} \\ \overset{*}{\overline{\Gamma}}_{2i} \\ f_{3i}\overset{*}{\overline{\Gamma}}_{2i} + f_{4i}\overline{\Gamma}_{2i} + f_{5i} \\ \overset{*}{\overline{\Gamma}}_{m2i} \\ g_{1i}\overset{*}{\overline{\Gamma}}_{m2i} + g_{2i}\overline{\Gamma}_{m2i} + g_{3i} \end{Bmatrix}, \tag{42}$$

with aerodynamic state vector

$$\mathbf{q}_{aero\,i} \equiv \begin{Bmatrix} \overline{\Gamma}_{1i} \\ \overline{\Gamma}_{2i} \\ \overset{*}{\overline{\Gamma}}_{2i} \\ \overline{\Gamma}_{m2i} \\ \overset{*}{\overline{\Gamma}}_{m2i} \end{Bmatrix}. \tag{43}$$

Expressions for the *f* and *g* coefficients appearing in the aerodynamic state space equations are given in Appendix E.

The combined state vector is defined as

$$\mathbf{q} \equiv \begin{Bmatrix} \mathbf{q}_{struct} \\ \hline \mathbf{q}_{aero\,1} \\ \vdots \\ \mathbf{q}_{aero\,N} \end{Bmatrix}. \tag{44}$$

For N radial aerodynamic points, the resulting state space model will consist of a system of $2(L+M)+5N$ first order differential equations with, in general, time varying coefficients. These state variable equations are numerically integrated using a fourth and fifth order Runge-Kutta-Fehlberg algorithm, with the integrations performed with respect to rotor azimuth angle, ψ.

For the numerical case studies presented in this report, we have used one out-of-plane bending mode and three torsional modes. Here, $W_1(\bar{x})$ was defined as

$$W_1 = \bar{x} = x/R, \tag{45}$$

which is the rigid body flapping deflection mode shape.

$\Phi_m(\bar{x})$ were assumed to be the first three torsional comparison functions developed by Karunamoorthy and Peters,[34] i.e.,

$$\begin{aligned} \Phi_1 &= 1, \\ \Phi_2 &= \frac{1}{2}\left(3\bar{x} - \bar{x}^3\right) \\ \Phi_3 &= \frac{1}{8}\left(30\bar{x}^2 - 15\bar{x}^4 - 7\right) \end{aligned} \quad . \tag{46}$$

The odd numbered torsional comparison functions in Equation 46 have been found to be good approximations of the exact torsional nonrotating mode shapes for pinned blade-root boundary conditions. The even numbered polynomials approximate the cantilevered boundary condition nonrotating mode shapes. Use of polynomial approximations instead of the exact nonrotating mode shapes is done solely to simplify calculation of the integral coefficients appearing in Equations 6 and 7.

4. RESULTS AND DISCUSSION

4.1 Piezoelectric twist actuated rotor blade conceptual design

Three conceptual piezoelectric induced twist rotor blade designs were examined in this study. These designs were developed in order to illustrate the twist actuation capabilities of the three general cases of piezoelectric actuation suggested by inspection of Equation 36. These three general cases are:

Case 1: $d_{31} \neq d_{33}$, $\tilde{c}_{11}^{E} = \tilde{c}_{22}^{E}$. This is the case of actuation lamina possessing piezoelectric free-strain anisotropy, and in-plane stiffness isotropy. This corresponds to a configuration where actuation layers are composed of solid, or monolithic, PZT materials, and are polarized according to the IDE scheme. This case will be referred to as IDE/MON for the remainder of the discussion.

Case 2: $d_{31} \neq d_{33}$, $\tilde{c}_{11}^{E} \neq \tilde{c}_{22}^{E}$. This is the case where the actuation lamina possess both free-strain and stiffness anisotropy. This would be true of a piezoelectric fiber composite, interdigitated electrode actuation scheme. This case will be referred to as IDE/PFC.

Case 3: $d_{31} = d_{33}$, $\tilde{c}_{11}^{E} \neq \tilde{c}_{22}^{E}$. This is the case of free-strain isotropy (or near isotropy) but with stiffness anisotropy in the actuating layers. This would be the case for a piezoelectric fiber composite structure utilizing a conventional poling scheme, or a case similar to the Directionally Attached Piezoelectric scheme, originally proposed by Barret[12] and developed experimentally by Chen and Chopra.[13] This scheme will be refered to as DAP/PFC in the following sections.

Stiffness, inertial, and actuation parameters for three conceptual helicopter blade designs, each representing one of the three cases above, were developed using full-scale helicopter parameters similar to those of the Sikorsky H-34 main rotor blade. The H-34 main rotor blade is a relatively simple, closed-section spar structure, and was easily idealized as a rectangular box section for the purposes of this study. These baseline blade parameters are summarized in Table 5.

Structural parameters not identical to the baseline blade parameters are shown for each of the piezoelectric twist blade designs in Table 6. Uniform blade properties were assumed in each case for simplicity. The piezoelectric material thickness fractions, t_{PE},, given here were calculated assuming that the blade total mass of each design could be no greater than 120% of the baseline full-scale helicopter blade mass. (The choice of 120% was essentially arbitrary, but represents a reasonable weight constraint on the design of the conceptual piezoelectric twist blades.) As a result, the torsional natural frequencies of the blade structures vary somewhat from the baseline design. The resulting natural frequencies of all of the blade designs are given in Table 7. Aerodynamic parameters used for the numerical case studies were not varied between the designs and are shown in Table 8.

4.2 Numerical twist actuation authority results

Numerically generated twist actuation authority results for each of the three piezoelectric induced twist blade designs are shown in Figures 7-9. These results are for a typical one-g hovering flight condition, which corresponds to a thrust coefficient of C_T = 0.00465. One electrode segment

extending from $\bar{x} = 0{,}1$ is assumed for all three structures. A sinusoidal electric field input with linearly increasing frequency and peak amplitude of $E_{1\max}$ was used to generate the frequency responses (amplitude and phase with respect to the electric field input signal) shown in the figures. In these figures the elastic twist is defined as the difference between the elastic torsional deflection at the blade tip and that at the blade root.

Figure 7 illustrates the structural response of the IDE/MON case. A sustained oscillatory elastic twist magnitude of approximately ±1.25° to ±1.5° is generated for excitation frequencies below the first torsional frequency. At the first torsional resonance, which is predominately an elastic torsional response, the amplitude increases to approximately ±2.25°. A smaller torsional response occurs at the second and third torsional resonance frequencies.

The resonant response at the second and third torsional frequencies was found to vary widely depending on the amount of material and aerodynamic damping present in the structure. As the torsional aerodynamic damping, from Equation 14, is in general proportional to $\bar{b}^2$, the corresponding aerodynamic damping for these two modes is almost negligible. Some additional form of damping is desirable then at these higher frequencies to avoid unrealistically large torsional deflections. As such, a level of material damping equivalent to 0.5% of critical damping was assumed for each of the cases presented here.

The actuation results for the IDE/PFC lamina design are shown for the same flight condition in Figure 8. A level of actuation capability on the order of ±1° to ±1.25° of elastic twist below the first torsional resonance, and ±1.5° at the first torsional mode resonance frequency is shown here. This is a level of performance slightly less than that demonstrated with the IDE/MON configuration. Although this may seem to imply that monolithic PZT laminae are more desirable for inclusion in piezoelectric actuated structures, manufacturing and poling nonplanar composite structures with solid PZT layers may not be practical. Piezoelectric fibers on the other hand could be incorporated into complex composite aerospace structures using, for the most part, established fiber composite construction techniques.

Figure 9 displays the twist actuation capabilities of the DAP/PFC blade design. Structurally, the DAP/PFC blade is identical to the IDE/PFC blade design, although the DAP/PFC blade utilizes conventional poling of the piezoelectric fibers. Relatively low nonresonant twist actuation is demonstrated for this actuation case, i.e., around ±0.2° to ±0.25° of elastic twist.

Comparison of the elastic twist actuation response of all three cases is shown in Figure 10. The effect of the large free-strain anisotropies present in the IDE schemes on the magnitude of elastic twist is readily apparent. Both IDE poling cases exibit generally four to five times the twist actuation magnitudes of the conventionally poled configuration. Such magnitudes of elastic twist are generally regarded as being sufficient for practical use in a vibration reduction scheme using individually controllable blade twist.

5. CONCLUSIONS

A simple helicopter rotor blade aeroelasticity analysis was developed and used to numerically demonstrate the twist actuation potential of embedded piezoelectric actuators for three nominally full-scale helicopter rotor blade designs. It was numerically demonstrated that useful nonresonant levels of oscillatory blade twist, i.e., on the order of ±1°, can potentially be produced without the addition of an excessive amount of piezoelectric actuator mass or saturation of the piezoelectric actuator materials, using an interdigitated electrode poling scheme with either a piezoelectric fiber composite or monolithic PZT actuation design.

The analysis and numerical model in its present form (i.e., with rigid flapping, elastic torsion and stall aerodynamics), should be sufficient for an examination of the potential of piezoelectric twist actuation to alleviate high oscillatory control loads induced by blade stall flutter.[35] Such a study is underway by the authors. Improvements to this model, such as the addition of multiple flapwise bending modes and a simple nonuniform inflow model, are also being undertaken.

ACKNOWLEDGEMENT

The authors wish to express their sincere thanks to Dr. W. Keith Belvin of the Structural Dynamics Branch, NASA Langley Research Center, for his invaluable technical assistance and guidance throughout the preparation of this report.

REFERENCES

1. Loewy, R., "Helicopter Vibrations: A Technological Perspective," *Journal of the American Helicopter Society*, Vol. 29, No. 4,October 1984, pp. 4-30.
2. Reichart, G., "Helicopter Vibration Control - A Survey," Vertica, Vol. 5, No. 1, 1981, pp. 1-20.
3. Johnson, W., "Self-Tuning Regulators for Multicyclic Control of Helicopter Vibrations," NASA Technical Paper 1996, 1982.
4. Shaw, J., Albion, N., Hanker, E. J., and Teal, R. S., "Higher Harmonic Control: Wind Tunnel Demonstration of Fully Effective Vibratory Hub Force Suppression," *Journal of the American Helicopter Society*, Vol. 34, No. 1, January 1989, pp. 14-25.
5. Kretz, M., "Research in Multicyclic and Active Control of Rotary Wings," *Vertica*, Vol 1., 1976, pp. 95-105.
6. Ham, N., "A Simple System for Helicopter Individual-Blade-Control Using Modal Decomposition," *Vertica*, Vol. 4, 1980, pp. 23-28.
7. Ham, N., "Helicopter Individual Blade Control and its Applications," 39th Annual Forum of the American Helicopter Society, St. Louis, MO, May 1983.
8. Ham, N., "Helicopter Individual-Blade-Control Research at MIT 1977-1985," *Vertica*, Vol. 11, 1987, pp. 109-122.
9. Spangler, R. L., Jr. and Hall, S. R., "Piezoelectric Actuators for Helicopter Rotor Control," *AIAA/ASME/ASCE/AHS/ASC 31st Structural Dynamics and Materials Conference, Apr. 2-4, 1990, Technical Papers*, AIAA Paper No. 90-1076, 1990, pp.1589-1599.
10. Samak, D., Chopra, I., "A Feasibility Study to Build a Smart Rotor: Trailing Edge Flap Actuation," *SPIE Smart Structures and Materials Conference, Feb. 1-4 1993, Smart Structures and Intelligent Systems, Proceedings*, Vol. 1917, Part 1, 1993, pp. 225-237.
11. Giurgiutiu, V., Chaudhry, Z., Rogers, C., "Engineering Feasibility of Induced Strain Actuators for Rotor Blade Active Vibration Control," *Journal of Intelligent Material Systems and Structures*, Vol. 6, No. 5, pp. 583-597, September 1995.
12. Barrett, R., "Intelligent Rotor Blade Structures Development Using Directionally Attached Piezoelectric Crystals," M.S. thesis, University of Maryland, College Park, MD, 1990.
13. Chen, P., Chopra, I., "A Feasibility Study to Build a Smart Rotor: Induced Strain Actuation of Airfoil Twisting Using Piezoceramic Crystals," *SPIE Smart Structures and Materials Conference, Feb. 1-4 1993, Smart Structures and Intelligent Systems, Proceedings*, Vol. 1917, Part 1, 1993, pp. 238-254.
14. Rodgers, J., Hagood, N., "Manufacture of Adaptive Composite Plates Incorporating Piezoelectric Fiber Composite Plies," *36th AIAA/ASME/ASCE/AHS/ASC Structures, Structural Dynamics, and Materials Conference and AIAA/ASME Adaptive Structures Forum, Technical Papers, Part 5*, New Orleans, LA, April 10-13, 1995.
15. Bent, A., Hagood, N., and Rodgers, J., "Anisotropic Actuation with Piezoelectric Fiber Composites," *Journal of Intelligent Material Systems and Structures*, Vol. 6, May 1995, pp. 338-349.

16. Hagood, N., Kindel, R., Ghandi, K., and Gaudenzi, P., "Improving Transverse Actuation of Piezoceramics Using Interdigitated Surface Electrodes," *SPIE Smart Structures and Materials Conference, Feb. 1-4 1993, Smart Structures and Intelligent Systems, Proceedings,* Vol. 1917, Part 1, 1993, pp. 341-352.
17. Millot, T., Friedmann, P., "Vibration Reduction in Helicopter Rotors Using an Actively Controlled Partial Span Trailing Edge Flap Located on the Blade," NASA Contractor Report 4611, June 1994.
18. Lemnios, A., Dunn, F.,"Theoretical Study of Multicyclic Control of a Controllable Twist Rotor," USAAMRDL, Moffett Field, CA, NASA CR-151959, April 1976.
19. Wei, F. S., Weisbrich, A. L.,"Multicyclic Controllable Twist Rotor Data Analysis," NASA CR-152251, January 1979.
20. Dadone, L., Cowan, J., and McHugh, F., "Variable Camber Rotor Study," NASA Contractor Report 166382, August 1982.
21. Song, O., Librescu, L., "Vibrational Behavior of Rotating Helicopter Blades Incorporating Adaptive Capabilities," *SPIE Smart Structures and Materials Conference, Feb. 1-4 1993, Smart Structures and Intelligent Systems, Proceedings*, Vol. 1917, Part 1, 1993, pp. 354-367.
22. Nitzsche, F., Breitbach, E., "Using Adaptive Structures to Attenuate Rotary Wing Aeroelastic Response," Journal of Aircraft, Vol. 31, No. 5, 1994, pp. 1178-1188.
23. Kaza, K. R. V., and Kvaternik, R. G., "Nonlinear Aeroelastic Equations for Combined Flapwise Bending, Chordwise Bending, Torsion, and Extension of Twisted Nonuniform Rotor Blades in Forward Flight," NASA TM 74059, August 1977.
24. Duncan, W., "Galerkin's Method in Mechanics and Differential Equations," Aeronautical Research Council Report and Memo 1798, August 1937.
25. Tran, C.T., Petot, D., "Semi-Empirical Model for the Dynamic Stall of Airfoils in View of the Application to the Calculation of Responses of a Helicopter Blade in Forward Flight," *Vertica*, Vol. 5, No. 1, pp. 35-53, 1981.
26. Peters, D. A., "Toward a Unified Lift Model for Use in Rotor Blade Stability Analyses," *Journal of the American Helicopter Society*, Vol. 30, No. 3, pp. 32-42, July, 1985.
27. Petot, D., "Differential Equation Modelling of Dynamic Stall," *Recherche Aerospatiale*, Vol. 5, No. 5, 1989.
28. Chouchane, M., "Application of a Dynamic Stall Model to Rotor Trim and Aeroelastic Response," Ph.D. Thesis, Georgia Institute of Technology, Atlanta, GA, August 1989.
29. Peters, D. A., Chouchane, M., and Fulton, M., "Helicopter Trim with Flap-Lag-Torsion and Stall by an Optimized Controller," *Journal of Guidance, Control and Dynamics*, Vol. 13, No. 5, pp. 824-834, Sept.-Oct., 1990.
30. Tang, D., private communication to W. K. Wilkie, August 1995.
31. Gessow, A., and Meyers, G., C., Jr., *Aerodynamics of the Helicopter*, College Park Press, 1952.
32. Johnson, W., *Helicopter Theory*, Princeton University Press, 1980.
33. ANSI/IEEE Std 176-1987, IEEE Standard on Piezoelectricity, 1988.
34. Karunamoorthy, S., Peters, D., "Use of Heirarchical Elastic Blade Equations and Automatic Trim for Rotor Response," *Vertica,*Vol. 11, No. 1/2, 1987, pp. 233-248.

35. Ham, N., Young, M., "Torsional Oscillations of Helicopter Blades Due to Stall," *Journal of Aircraft*, Vol. 3, No. 3, pp. 218-224, May-June 1966.
36. Rehfield, L. W., "Design Analysis Methodology for Composite Rotor Blades," Seventh DoD/NASA Conference on Fibrous Composites in Structural Design, Denver CO, June 1985.
37. Jones, R. M., *Mechanics of Composite Materials*, McGraw-Hill, 1975.

APPENDIX A. COORDINATE SYSTEMS AND TRANSFORMATIONS

Several coordinate systems are used to describe the flap-torsion kinematics of the rotor blade. These coordinate systems are shown in Figure A1 , and described below.

1. $X_I Y_I Z_I$ is an inertial reference frame with origin at the hub center of rotation, X_I axis oriented in the direction of forward flight, and negative Z_I axis aligned with the rotor rotation vector.

2. $X_1 Y_1 Z_1$ is a hub-fixed rotating reference frame, with the Z_1 axis in the direction of the rotor rotation vector. The $X_1 Y_1 Z_1$ system is rotated about the Z_0 axis by the blade azimuth angle ψ. The X_1 axis is coincident with the undeformed blade elastic axis.

3. $x_0 y_0 z_0$ is a blade-fixed reference system located at an arbitrary point (x) along the blade undeformed elastic axis.

4. xyz is a reference system fixed in the deformed blade, and translated with respect to the $x_0 y_0 z_0$ system.

5. $x_2 y_2 z_2$ is an intermediate system obtained by rotation of the xyz system about y by the angle w'.

6. $x_3 y_3 z_3$ is a reference system fixed in the deformed blade obtained by rotating the $x_2 y_2 z_2$ system about y_2 by the total rotation angle $\theta = \theta_{con} + \phi$. x_3 is tangent to the deformed elastic axis.

Coordinate transformations due to rotations between the various systems are given below.

Transformation from the inertial system ($X_I Y_I Z_I$) to hub-fixed rotating system($X_1 Y_1 Z_1$):

$$ {}^1\mathbf{T}_0 = \begin{bmatrix} -\cos\psi & \sin\psi & 0 \\ \sin\psi & \cos\psi & 0 \\ 0 & 0 & -1 \end{bmatrix} \tag{A1} $$

Transformation from the blade-fixed xyz system to the intermediate deformed system $x_2 y_2 z_2$ (rotation about y by w'):

$$ {}^2\mathbf{T}_1 = \begin{bmatrix} \cos w' & 0 & \sin w' \\ 0 & 1 & 0 \\ -\sin w' & 0 & \cos w' \end{bmatrix} \tag{A2} $$

Transformation from the $x_2y_2z_2$ system to the $x_3y_3z_3$ system (rotation about y_2 by θ):

$$ {}^{3}\mathbf{T}_{2} = \begin{bmatrix} 1 & 0 & 0 \\ 0 & \cos\theta & \sin\theta \\ 0 & -\sin\theta & \cos\theta \end{bmatrix} \tag{A3} $$

APPENDIX B. GENERALIZED FORCE DISPLACEMENT RELATIONS FOR A COMPOSITE THIN WALLED BEAM STRUCTURE

Rehfield[36] presents a general theory for characterizing the structural properties of thin walled composite beam structures. Portions of this theory necessary for deriving the beam stiffness properties of an idealized rectangular thin walled rotor blade structure are given below.

Membrane resultant stresses and strains for a composite laminate are related by the membrane stiffness matrix, *A*, as follows,

$$\begin{Bmatrix} N_1 \\ N_2 \\ N_6 \end{Bmatrix} = \begin{bmatrix} A_{11} & A_{12} & A_{16} \\ A_{12} & A_{22} & A_{26} \\ A_{16} & A_{26} & A_{66} \end{bmatrix} \begin{Bmatrix} S_1^0 \\ S_2^0 \\ S_6^0 \end{Bmatrix} \tag{B1}$$

The elements of A are formed from the individual laminate plane stress stiffnesses according to Classical Laminated Plate Theory[37], i.e.,

$$A_{ij} = \sum_{k=1}^{n} \left(c_{ij}^{E} \right)_k t_k \ , \qquad (i, j = 1,2,6), \tag{B2}$$

where n is the number of plies of the laminate.

With the assumption that the hoop stress, N_2, is zero, the hoop strain, S_2^0, may be written as

$$S_2^0 = \frac{\left(A_{12} S_1^0 + A_{26} S_6^0 \right)}{A_{22}}. \tag{B3}$$

Applying equation B3 to B1, and rewritting the extensional and shear stresses in terms of the remaining strains yields

$$\begin{Bmatrix} N_1 \\ N_6 \end{Bmatrix} = \begin{bmatrix} K_{11} & K_{12} \\ K_{12} & K_{22} \end{bmatrix} \begin{Bmatrix} S_1^0 \\ S_6^0 \end{Bmatrix}, \tag{B4}$$

where the K stiffnesses are given by

$$K_{11} = A_{11} - \frac{(A_{12})^2}{A_{22}},$$

(B5)

$$K_{12} = A_{16} - \frac{A_{12}A_{26}}{A_{22}},$$

(B6)

$$K_{22} = A_{66} - \frac{(A_{26})^2}{A_{22}}.$$

(B7)

The relation between the generalized elastic beam forces and generalized displacements used in the blade equations of motion of this paper may then be expresed as

$$\begin{Bmatrix} N_x \\ M_x \\ M_y \end{Bmatrix} = \begin{bmatrix} C_{11} & C_{14} & C_{15} \\ C_{14} & C_{44} & C_{45} \\ C_{15} & C_{45} & C_{55} \end{bmatrix} \begin{Bmatrix} u' \\ \phi' \\ w'' \end{Bmatrix}$$

(B8)

The elements of matrix C correspond to the beam stiffnesses of the blade equations of motion as follows:

$$C_{11} = \oint K_{11} ds \approx EA,$$

(B9)

$$C_{44} = \frac{4A_e^{\,2}}{c^2} \oint K_{22} ds \approx GJ,$$

(B10)

$$C_{55} = \oint K_{11} z^2 ds \approx EI_{\eta\eta},$$

(B11)

$$C_{14} = \frac{2A_e}{c} \oint K_{12} ds.$$

(B12)

Integrations in equations B9-12 are performed around the contour of the beam section, with A_e the area enclosed by the contour perimeter, and c the contour length.

For the blade structural configurations discussed in this paper, coupling stiffnesses C_{15} and C_{45} are identically zero. The extension-torsion coupling stiffness, C_{14}, is zero for the monolithic PZT actuation structure. The fiber composite structures will inherently contain

some extension twist coupling, resulting in a nonzero C_{14}. This coupling, however, is relatively small for the particular configurations studied in this paper and was not included in the blade equations of motion. Future, more extensive, developments of the blade equations will include these elastic couplings.

APPENDIX C. DEFINITION OF SECTION ANGLE OF ATTACK AND SECTION ROTATION RATE WITH RESPECT TO THE AIR MASS

C.1 Section angle of attack:

The two dimensional angle of attack of the ith airfoil section (α_i) is defined by

$$\alpha_i = \tan^{-1}\left(\frac{U_Y}{U_X}\right)_i \tag{C1.1}$$

where U_X and U_Y (omitting subscripts) are the components of the nondimensional section airflow velocity normal and parallel to the section chord. U_X and U_Y expressed in the customary airfoil coordinate system (Figure C1) are

$$U_X \equiv \frac{-V_y}{\Omega R} = -U_y, \qquad U_Y \equiv \frac{V_z}{\Omega R} = U_z; \tag{C1.2}$$

with the total nondimensional section airflow velocity given by

$$U = \sqrt{U_X{}^2 + U_Y{}^2}\ . \tag{C1.3}$$

Spanwise flow, i.e., flow in the x_3 direction is neglected.

V_z and V_y are the components of the section airfoil velocity with respect to the air mass in the $x_3y_3z_3$ system (see Appendix A), viz.

$$\mathbf{V} = \begin{Bmatrix} V_x \\ V_y \\ V_z \end{Bmatrix} = {}^3\mathbf{V}_a - {}^3\mathbf{V}_b$$

$$= {}^3\mathbf{T}_2\,{}^2\mathbf{T}_1\,{}^1\mathbf{T}_0\,{}^0\mathbf{V}_a - {}^3\mathbf{T}_2\,{}^2\mathbf{T}_1\,{}^1\mathbf{V}_b \tag{C1.4}$$

${}^0\mathbf{V}_a$ and ${}^1\mathbf{V}_b$ are, respectively, the velocity of the air mass in the inertial system, and the velocity of the airfoil section due to blade motion with respect to the $x_0y_0z_0$ system, given by

$$ {}^{0}\mathbf{V}_a = \begin{Bmatrix} -V_\infty \cos\alpha_s \\ 0 \\ \nu \end{Bmatrix}, \qquad {}^{1}\mathbf{V}_b = \begin{Bmatrix} 0 \\ r\Omega \\ r\dot{w}' \end{Bmatrix} $$

(C1.5)

Making appropriate small angle assumptions for α_s, w', and θ (and implicitly for θ_{con} and ϕ), yields for **V**:

$$ \begin{Bmatrix} V_x \\ V_y \\ V_z \end{Bmatrix} = \begin{Bmatrix} V_\infty \cos\psi - \nu w' \\ -V_\infty \sin\psi - V_\infty w'\theta \cos\psi - \nu\theta \\ V_\infty \theta \sin\psi - V_\infty w' \cos\psi - \nu \end{Bmatrix} - \begin{Bmatrix} xw'\dot{w}' \\ x\Omega + x\dot{w}'\theta \\ -x\Omega\theta + x\dot{w}' \end{Bmatrix} $$

$$ = \begin{Bmatrix} V_\infty \cos\psi - \nu w' x - xw'\dot{w}' \\ -V_\infty \left(w'\theta \cos\psi + \sin\psi\right) - \nu\theta - x\left(\Omega + \dot{w}'\theta\right) \\ V_\infty \left(\theta \sin\psi - w' \cos\psi\right) - \nu + x\left(\Omega\theta - \dot{w}'\right) \end{Bmatrix} $$

(C1.6)

Dividing by ΩR yields the components of the nondimensional section velocity in the blade coordinate system (3-system)

$$ \begin{Bmatrix} U_x \\ U_y \\ U_z \end{Bmatrix} = \begin{Bmatrix} \mu \cos\psi - \left(\lambda_{TPP} w^+ + w^+ \overset{*}{w}^+\right)\bar{x} \\ -\mu \sin\psi - \mu w^+ \theta \cos\psi - \lambda_{TPP}\theta - \bar{x}\left(1 + \overset{*}{w}^+ \theta\right) \\ \mu\theta \sin\psi - \mu w^+ \cos\psi - \lambda_{TPP} + \bar{x}\left(\theta - \overset{*}{w}^+\right) \end{Bmatrix}, $$

(C1.7)

where (*) denotes differentiation with respect to the rotor azimuth, and ($^+$) differentiation with respect to *x/R*. Substituting U_z and U_y into equation C1.1 and then into equation C1.2 yields the section angles of attack.

C.2: Section rotation rate:

The rotation rate of the airfoil section with respect to the air mass will be defined as

$$ \overset{*}{\varepsilon} \equiv \frac{d\varepsilon}{d\psi} = \overset{*}{\varepsilon}_\theta + \overset{*}{\varepsilon}_{w'}, $$

(C2.1)

where $\overset{*}{\varepsilon}_\theta$ is the rotation rate of the airfoil due to blade pitch motion, and $\overset{*}{\varepsilon}_{w'}$ is the effective rate rotation of the airfoil due to the component of the rotor rotation vector lying along the section pitch axis, x_3.

$\overset{*}{\varepsilon}_\theta$ is given simply by

$$\overset{*}{\varepsilon}_\theta \equiv \frac{\partial \theta}{\partial \psi} = \overset{*}{\theta} = \overset{*}{\theta}_{con} + \overset{*}{\phi}. \tag{C2.2}$$

$\overset{*}{\varepsilon}_{w'}$ may be found by examination of the vector component of the rotor rotation lying along the x_3, i.e.,

$$\dot{\varepsilon}_{w'} = \frac{\partial \psi}{\partial t}\frac{\partial \varepsilon_{w'}}{\partial \psi} = \Omega \overset{*}{\varepsilon}_{w'} = \Omega \mathbf{k}_1 \cdot \mathbf{i}_3, \tag{C2.3}$$

where $\mathbf{k}_1$ is a unit vector in the direction of the positive Z_1 axis, and $\mathbf{i}_3$ a unit vector in the direction of the positive x_3 axis. Rewriting C2.3 yields

$$\overset{*}{\varepsilon}_{w'} = \mathbf{k}_1 \cdot \mathbf{i}_3 = \sin w' \cong w^+, \tag{C2.4}$$

for small rotations.

The total rotation rate with respect to the air mass may then be written as

$$\overset{*}{\varepsilon} = \overset{*}{\theta}_{con} + \overset{*}{\phi} + w^+. \tag{C2.5}$$

APPENDIX D. SYSTEM MATRICES

Equations 6 and 7 may be rewritten as a system of $M + N$ ordinary differential equations of the form

$$M\overset{**}{\mathbf{x}} + C\overset{*}{\mathbf{x}} + K\mathbf{x} = \bar{\mathbf{f}}_{aero} + \bar{\mathbf{f}}_{PE} + \bar{\mathbf{f}}_{\theta} ,$$

(D1)

where **x** is a vector of structural generalized displacements, given by

$$\mathbf{x} = \left\{ \overline{w}_1 \quad \overline{w}_2 \quad \cdots \quad \overline{w}_L \quad \phi_1 \quad \phi_2 \quad \cdots \quad \phi_M \right\}^T .$$

(D2)

The symmetric mass matrix, M, in equation D1 is given by

$$M = \begin{bmatrix} \left[I^{00} \right] & \left[J^{00} \right] \\ \left[J^{00} \right]^T & \left[K^{00} \right] \end{bmatrix},$$

(D3)

with

$$I^{00} = \begin{bmatrix} I_{11}^{00} & I_{12}^{00} & \cdots & I_{1L}^{00} \\ I_{21}^{00} & I_{22}^{00} & & \vdots \\ \vdots & & \ddots & \vdots \\ I_{L1}^{00} & \cdots & \cdots & I_{LL}^{00} \end{bmatrix},$$

(D4)

$$I_{mn}^{00} \equiv \int_0^1 W_m W_n d\bar{x} ,$$

(D5)

$$J^{00} = \begin{bmatrix} J_{11}^{00} & J_{12}^{00} & \cdots & J_{1M}^{00} \\ J_{21}^{00} & J_{22}^{00} & & \vdots \\ \vdots & & \ddots & \vdots \\ J_{L1}^{00} & \cdots & \cdots & J_{LM}^{00} \end{bmatrix},$$

(D6)

$$J_{mn}^{00} \equiv \int_0^1 \bar{e} W_m \Phi_n d\bar{x}$$

(D7)

$$K^{00} = \begin{bmatrix} K_{11}^{00} & K_{12}^{00} & \cdots & K_{1M}^{00} \\ K_{21}^{00} & K_{22}^{00} & & \vdots \\ \vdots & & \ddots & \vdots \\ K_{M1}^{00} & \cdots & \cdots & K_{MM}^{00} \end{bmatrix},$$

(D8)

$$K_{mn}^{00} \equiv \int_0^1 \frac{k_m{}^2}{R^2} \Phi_m \Phi_n d\bar{x} \,.$$

(D9)

C is a symmetric structural damping matrix,

$$C = \begin{bmatrix} \left[{}^*I^{22} \right] & [0] \\ [0] & \left[{}^*K^{11} \right] \end{bmatrix},$$

(D10)

with

$${}^*I^{22} = \begin{bmatrix} {}^*I_{11}^{22} & {}^*I_{12}^{22} & \cdots & {}^*I_{1L}^{22} \\ {}^*I_{21}^{22} & {}^*I_{22}^{22} & & \vdots \\ \vdots & & \ddots & \vdots \\ {}^*I_{L1}^{22} & \cdots & \cdots & {}^*I_{LL}^{22} \end{bmatrix},$$

(D11)

$${}^*I_{mn}^{22} \equiv \int_0^1 \frac{E^* I_{\eta\eta}}{m\Omega R^4} W_m{}^{++} W_n{}^{++} d\bar{x} \,,$$

(D12)

$${}^*K^{11} = \begin{bmatrix} {}^*K_{11}^{11} & {}^*K_{12}^{11} & \cdots & {}^*K_{1M}^{11} \\ {}^*K_{21}^{11} & {}^*K_{22}^{11} & & \vdots \\ \vdots & & \ddots & \vdots \\ {}^*K_{M1}^{11} & \cdots & \cdots & {}^*K_{MM}^{11} \end{bmatrix},$$

(D13)

$${}^*K_{mn}^{11} \equiv \int_0^1 \frac{G^* J}{m\Omega R^4} \Phi_m{}^{+} \Phi_n{}^{+} d\bar{x} \,.$$

(D14)

K is a linear stiffness matrix of the form

$$K = \begin{bmatrix} \left[I^{WW}\right] & \left[{}_1J^{10}\right] \\ \left[{}_1J^{10}\right]^T & \left[K^{\Phi\Phi}\right] \end{bmatrix}, \tag{D15}$$

where

$$I^{WW} = \begin{bmatrix} \left({}^TI_{11}^{11} + {}^0I_{11}^{11} + I_{11}^{22}\right) & \cdots & \left({}^TI_{1L}^{11} + {}^0I_{1L}^{11} + I_{1L}^{22}\right) \\ \vdots & \ddots & \vdots \\ \left({}^TI_{L1}^{11} + {}^0I_{L1}^{11} + I_{L1}^{22}\right) & \cdots & \left({}^TI_{LL}^{11} + {}^0I_{LL}^{11} + I_{LL}^{22}\right) \end{bmatrix}, \tag{D16}$$

$${}^TI_{mn}^{11} \equiv \int_0^1 \frac{T}{m\Omega^2 R^2} W_m{}^+ W_n{}^+ d\bar{x}\,, \tag{D17}$$

$${}^0I_{mn}^{11} \equiv \frac{K_\beta}{\Omega^2 R^2 \int_0^1 m d\bar{x}} W_m{}^+(0) W_n{}^+(0), \tag{D18}$$

$$I_{mn}^{22} \equiv \int_0^1 \frac{EI_{\eta\eta}}{m\Omega^2 R^4} W_m{}^{++} W_n{}^{++} d\bar{x}\,, \tag{D19}$$

$${}_1J^{10} = \begin{bmatrix} {}_1J_{11}^{10} & \cdots & {}_1J_{1M}^{10} \\ \vdots & \ddots & \vdots \\ {}_1J_{L1}^{10} & \cdots & {}_1J_{LM}^{10} \end{bmatrix}, \tag{D20}$$

$${}_1J_{mn}^{10} \equiv \int_0^1 \bar{e}\bar{x} W_m{}^+ \Phi_n d\bar{x}\,, \tag{D21}$$

$$K^{\Phi\Phi} = \begin{bmatrix} \left(K_{11}^{00} + {}^TK_{11}^{00} + K_{11}^{11} + {}^0K_{11}^{00}\right) & \cdots & \left(K_{1M}^{00} + {}^TK_{1M}^{00} + K_{1M}^{11} + {}^0K_{1M}^{00}\right) \\ \vdots & \ddots & \vdots \\ \left(K_{M1}^{00} + {}^TK_{M1}^{00} + K_{M1}^{11} + {}^0K_{M1}^{00}\right) & \cdots & \left(K_{MM}^{00} + {}^TK_{MM}^{00} + K_{MM}^{11} + {}^0K_{MM}^{00}\right) \end{bmatrix}, \tag{D22}$$

$$K_{mn}^{00} \equiv \int_0^1 \frac{k_m{}^2}{R^2} \Phi_m \Phi_n d\bar{x}\,, \tag{D23}$$

$${}^TK_{mn}^{11} \equiv \int_0^1 \frac{T}{m\Omega^2 R^2} \frac{k_A{}^2}{R^2} \Phi_m{}^+ \Phi_n{}^+ d\bar{x}\,, \tag{D24}$$

$$K_{mn}^{11} \equiv \int_0^1 \frac{GJ}{m\Omega^2 R^4} \Phi_m{}^+ \Phi_n{}^+ d\bar{x}\,,$$

(D25)

$${}^0K_{mn}^{00} \equiv \frac{K_\theta}{\Omega^2 R^2 \int_0^1 m d\bar{x}} \Phi_m(0)\Phi_n(0).$$

(D26)

$\bar{f}_{aero}$, $\bar{f}_{PE}$ and $\bar{f}_{\theta_0}$ are, repectively, the nondimensional aerodynamic forces, nondimensional piezoelectric induced twisting moments, and nondimensional steady state inertial propeller moments, and are shown below:

$$\bar{\mathbf{f}}_{aero} = \begin{Bmatrix} \int_0^1 \overline{L}_w W_1 d\bar{x} \\ \vdots \\ \int_0^1 \overline{L}_w W_L d\bar{x} \\ \int_0^1 \overline{M}_\phi \Phi_1 d\bar{x} \\ \vdots \\ \int_0^1 \overline{M}_\phi \Phi_M d\bar{x} \end{Bmatrix},$$

(D27)

$$\overline{L}_w \equiv \frac{L_w}{m\Omega^2 R},$$

(D28)

$$\overline{M}_\phi \equiv \frac{M_\phi}{m\Omega^2 R^2},$$

(D29)

$$\bar{\mathbf{f}}_{PE} = \begin{Bmatrix} 0 \\ \vdots \\ 0 \\ \int_0^1 \overline{Q}_{PE} \Phi_1^+ d\bar{x} \\ \vdots \\ \int_0^1 \overline{Q}_{PE} \Phi_M^+ d\bar{x} \end{Bmatrix},$$

(D30)

$$\overline{Q}_{PE} \equiv \frac{Q_{PE}}{m\Omega^2 R^2},$$

(D31)

$$\bar{\mathbf{f}}_\theta = -\begin{Bmatrix} J_1^0 \\ \vdots \\ J_L^0 \\ K_1^0 \\ \vdots \\ K_M^0 \end{Bmatrix} \overset{**}{\theta} - \begin{Bmatrix} {}_1J_1^1 \\ \vdots \\ {}_1J_L^1 \\ K_1^0 \\ \vdots \\ K_M^0 \end{Bmatrix} \theta \,, \tag{D32}$$

$$J_m^0 \equiv \int_0^1 \bar{e} W_m \, d\bar{x} \,, \tag{D33}$$

$${}_1J_m^1 \equiv \int_0^1 \bar{e}\bar{x} W_m{}^+ \, d\bar{x} \,, \tag{D34}$$

$$K_m^0 \equiv \int_0^1 \frac{k_m{}^2}{R^2} \Phi_m \, d\bar{x} \,. \tag{D35}$$

APPENDIX E. AERODYNAMIC STATE SPACE COEFFICIENTS

Coefficients associated with lift formulation:

$$f_1 = -\frac{\lambda_z}{\bar{k}} \tag{E1}$$

$$f_2 = \left(a\lambda_z U_y + \bar{b}\varepsilon'\delta_z\right)/\bar{k} \tag{E2}$$

$$f_3 = -2d_z w_z/\bar{k} \tag{E3}$$

$$f_4 = -w_z{}^2\left(1 + d_z{}^2\right)/\bar{k}^2 \tag{E4}$$

$$f_5 = f_4\left(U_X \Delta C_z + e_z \bar{k}\left(\overset{*}{U}_X \Delta C_z + \frac{\partial \Delta C_z}{\partial \alpha}\overset{*}{U}_Y\right)\right) \tag{E5}$$

Coefficients associated with pitching moment formulation:

$$g_1 = -a_m/\bar{k} \tag{E6}$$

$$g_2 = -r_m/\bar{k}^2 \tag{E7}$$

$$g_3 = g_2 U \Delta C_m - E_m \overset{*}{U}_Y/\bar{k}\,. \tag{E8}$$

Table 1. Ordering of nondimensional parameters appearing in equations of motion. ($\varepsilon \equiv 0.10$).

$u/R = O(\varepsilon^2)$	$EI/m\Omega^2 R^4 = O(\varepsilon^3)$
$v/R = O(\varepsilon^2)$	$G/m\Omega^2 = O(\varepsilon^{-6})$
$w/R = O(\varepsilon)$	$EA/m\Omega^2 R^2 = O(\varepsilon^{-2})$
$\phi = O(\varepsilon)$	$k_A^2/R^2 = O(\varepsilon^4)$
$\theta = O(\varepsilon)$	$k_m^2/R^2 = O(\varepsilon^4)$
$e/R = O(\varepsilon^3)$	$B_1^*/AR^4 = O(\varepsilon^4)$
$e_A/R = O(\varepsilon^3)$	$B_2^*/AR^3 = O(\varepsilon^3)$
$x/R = O(1)$	$J/R^4 = O(\varepsilon^9)$

Table 2. Lift based ONERA stall coefficients for the OA212 airfoil.

Parameter	Value	Physical Description
λ	0.2	time delay parameter
s	5	apparent mass quantity
δ	$\frac{\partial C_z}{\partial \alpha} - 4\left(1 + 1.43\Delta C_z\right)$	lift coefficient to pitch rate relation
w	$0.10 + 0.023\left(\lvert\alpha\rvert - 13^\circ\right)u\left(\lvert\alpha\rvert - 13^\circ\right), \quad \lvert\alpha\rvert < 21.7^\circ$ $0.3, \quad \lvert\alpha\rvert > 21.7^\circ$	damping factor (u is a unit step function.)
d	$0.105/w$	stall natural frequency
e	$2 - 5.1\tan^{-1}\left[1.21\left(\lvert\alpha\rvert - 13^\circ\right)\right]u\left(\lvert\alpha\rvert - 13^\circ\right)$	phase shift parameter

Table 3. Coefficients for stalled pitching moment circulation equation. Values are for the "mean airfoil" of Reference 27.

Parameter	Value
r_0	0.2
r_2	0.2
a_0	0.25
a_2	0.1
E_2	0.573

Table 4. Lamina structural properties. Piezoelectric lamina properties are derived from values reported by Rogers and Hagood.

Property	passive blade structure	monolithic PZT lamina	IDE/PFC lamina	DAP/PFC lamina
c_{11}	12.8e6 psi	9.6e6 psi	4.5e6 psi	4.5e6 psi
c_{22}/c_{11}	1	1	0.60	0.60
c_{12}/c_{11}	0.375	0.29	0.24	0.24
c_{66}	4.0e6 psi	3.4e6 psi	8.3e5	8.3e5
d_{31}/d_{33}	-	-0.5	-0.4	1
ρ	0.1 lbs/in^3	0.27 lbs/in^3	0.21 lbs/in^3	0.21 lbs/in^3
Λ_{max}	-	500 $\mu\varepsilon$	500 $\mu\varepsilon$	250 $\mu\varepsilon$

Table 5. Baseline helicopter rotor parameters.

Parameter	Baseline blade value
Ω (rad/sec)	23.2
R (in)	336
γ	9.44
c/R	0.0488
n	4
σ	0.0622
C_T	0.00465
$f/\pi R^2$	0.015
$\overline{\omega}_\theta = \sqrt{K_\theta / \Omega^2 I_\theta}$	16.0
m (slinch/in)	0.00142
mk_m^2 (slinch-in^2/in)	0.0175
I_θ / I_β	0.000327
e/c	0
$\frac{GJ}{I_\beta \Omega^2 R}$	0.00552
h (in)	1.84
w (in)	6.11
t (in)	0.141

Table 6. Structural parameters for numerical examples.

Parameter	IDE/MON	IDE/PFC	DAP/PFC
$\frac{GJ}{I_\beta \Omega^2 R}$	0.00447	0.00365	0.00365
γ	8.28	8.28	8.28
t_{PE}/t	0.1875	0.300	0.300

Table 7. Calculated nondimensional blade natural frequencies for numerical examples.

Parameter	Baseline blade value	IDE/MON	IDE/PFC	DAP/PFC
$\overline{\omega}_{\beta}$	1.0	1.0	1.0	1.0
$\overline{\omega}_{\phi_1}$	6.10	5.60	5.14	5.14
$\overline{\omega}_{\phi_2}$	18.19	16.64	15.22	15.22
$\overline{\omega}_{\phi_3}$	61.02	59.67	58.58	58.58

Table 8. Aerodynamic parameters for numerical examples.

Parameter	value
c_1	$-\frac{\pi}{4}\left(1+1.4M^2\right)$
c_2	$\approx c_1$
c_3	$-\frac{3\pi}{16}\left(-1.26-1.53\tan^{-1}\left(15(M-0.7)\right)\right)$
M	0.30
$\bar{y}_{ac}$	0
N	5
$\bar{x}$	{0.28 0.44 0.60 0.76 0.92}
Δ	{0.16 0.16 0.16 0.16 0.16}

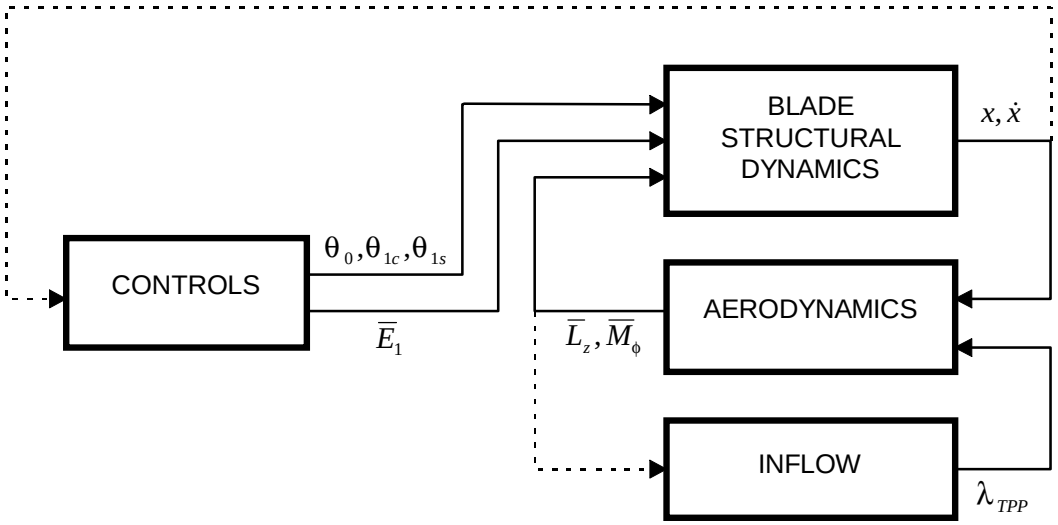

Figure 1. Conceptual diagram for a unified rotor blade piezoelectric aeroelastic analysis.

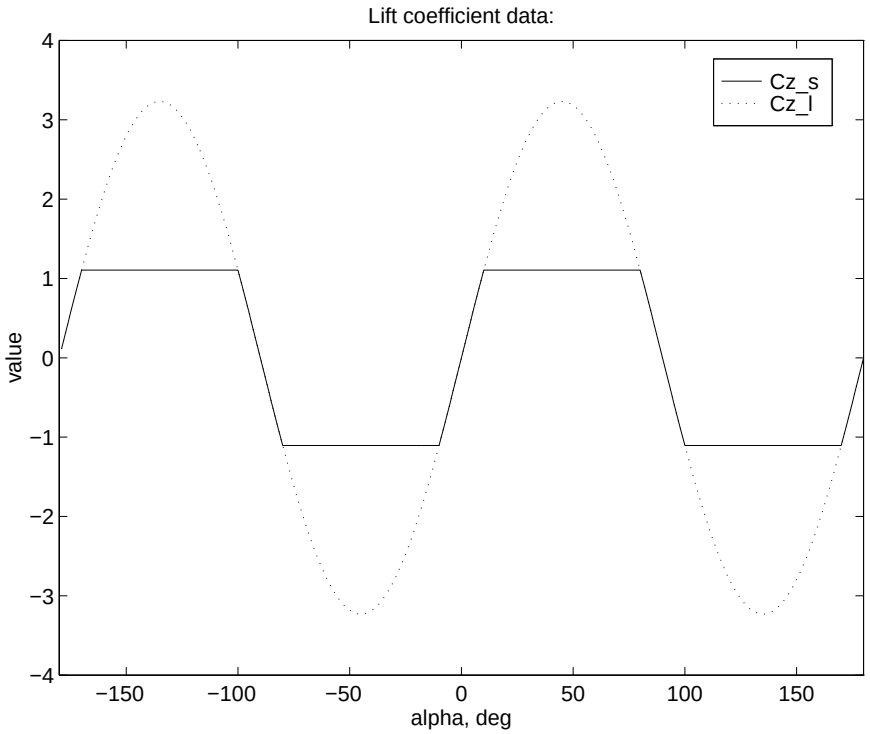

Figure 2. Static lift coefficient curves (linear model and stalled) for the OA212 airfoil.

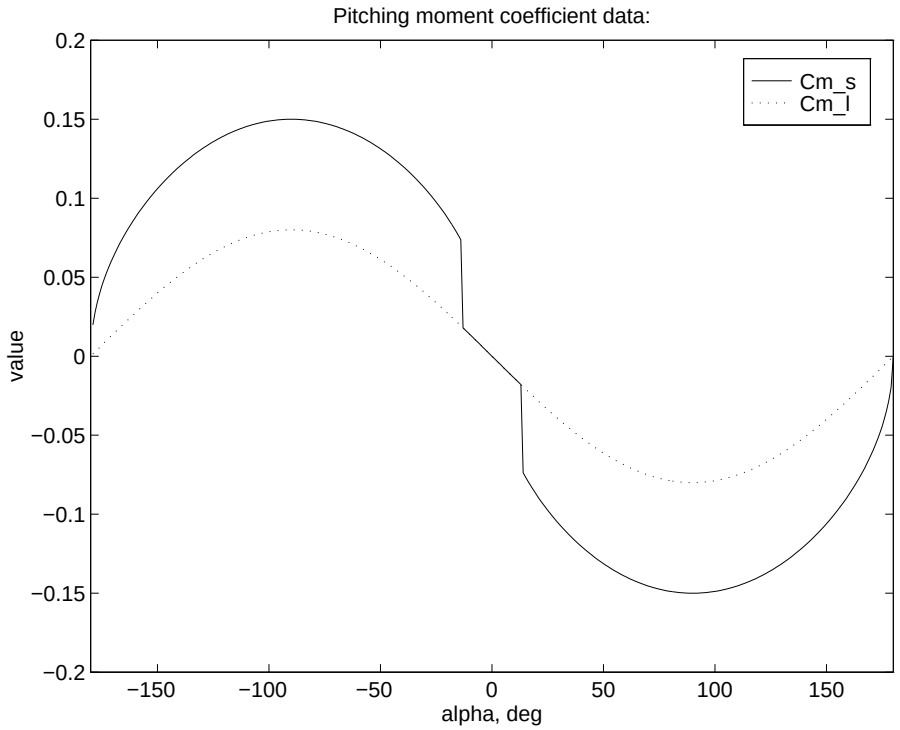

Figure 3. Static pitching moment curves (linear model and stalled) for the OA212 airfoil.

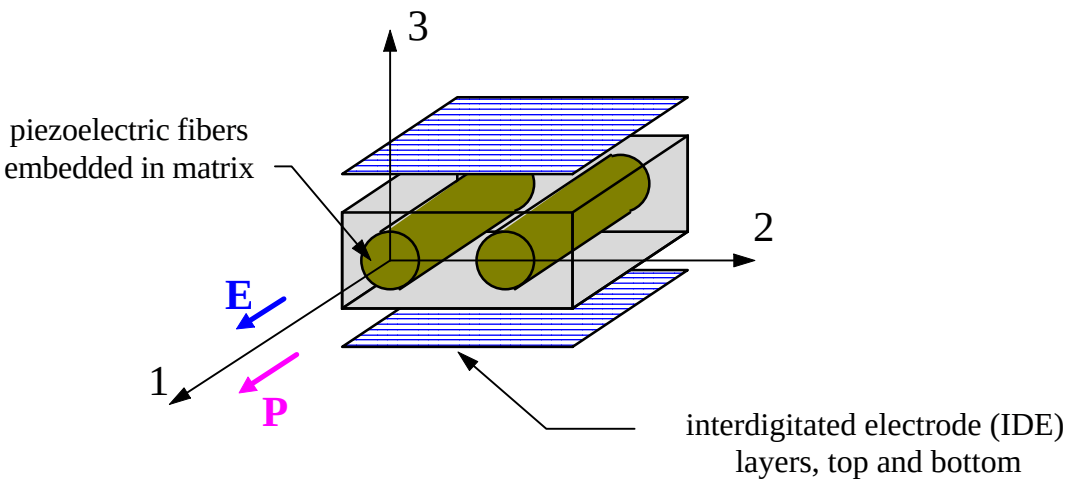

Figure 4. Material axis system for piezoelectric fiber composite assuming interdigitated electrode poling scheme.

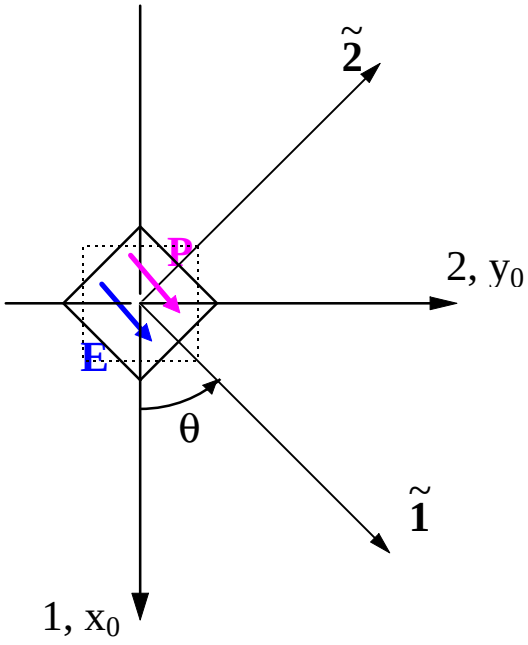

Figure 5. Rotation of piezoelectric fiber composite material system with respect to the global (blade) system.

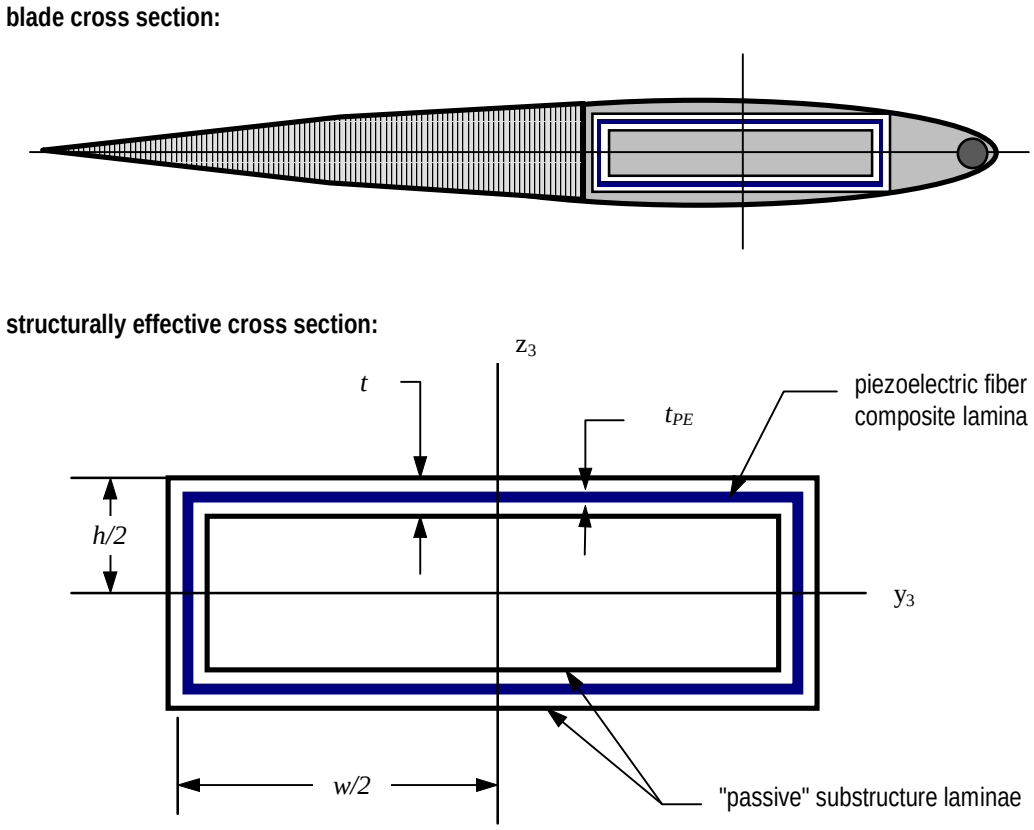

Figure 6. Idealized rectangular, thin-walled, closed-section piezoelectric blade structure.

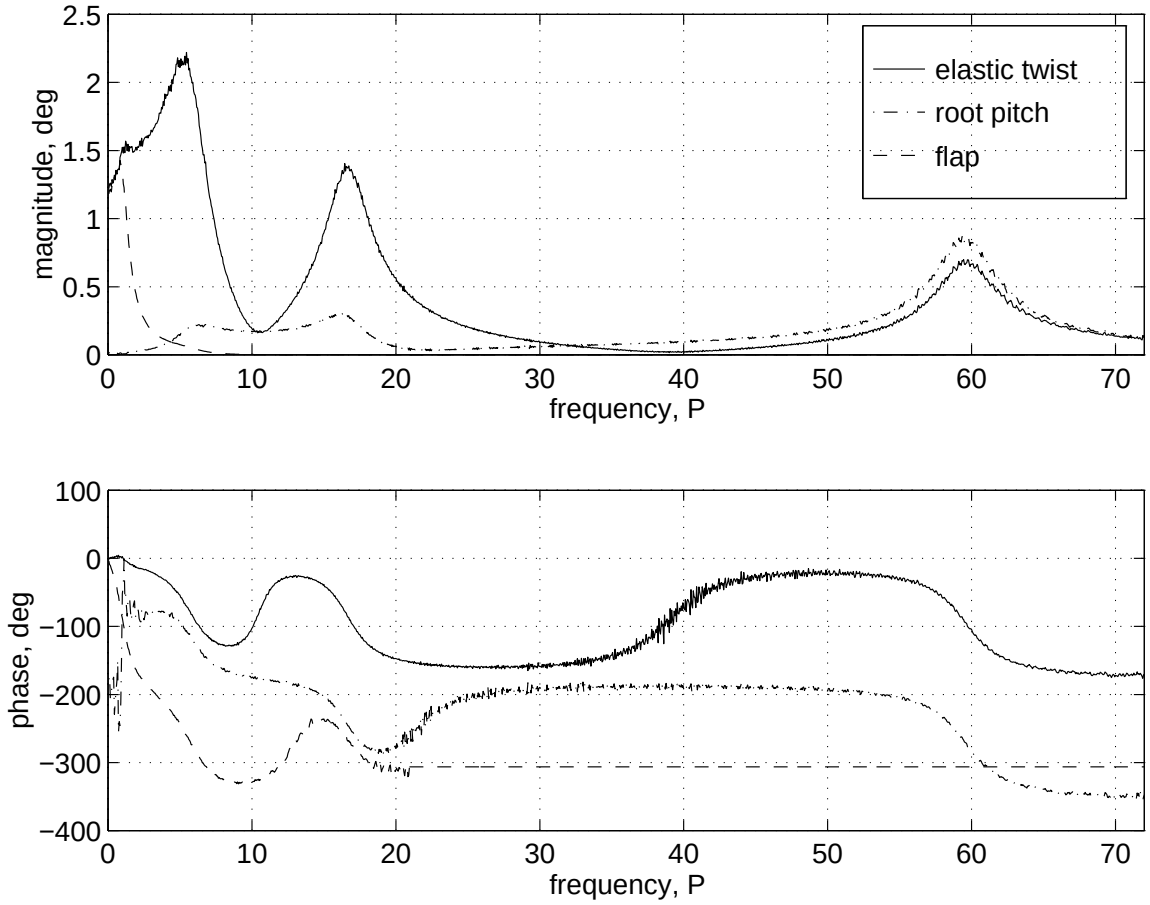

Figure 7. Blade frequency response: monolithic PZT (MON) twist actuation with interdigitated electrode poling scheme; C_T = 0.00465, μ = 0.0.

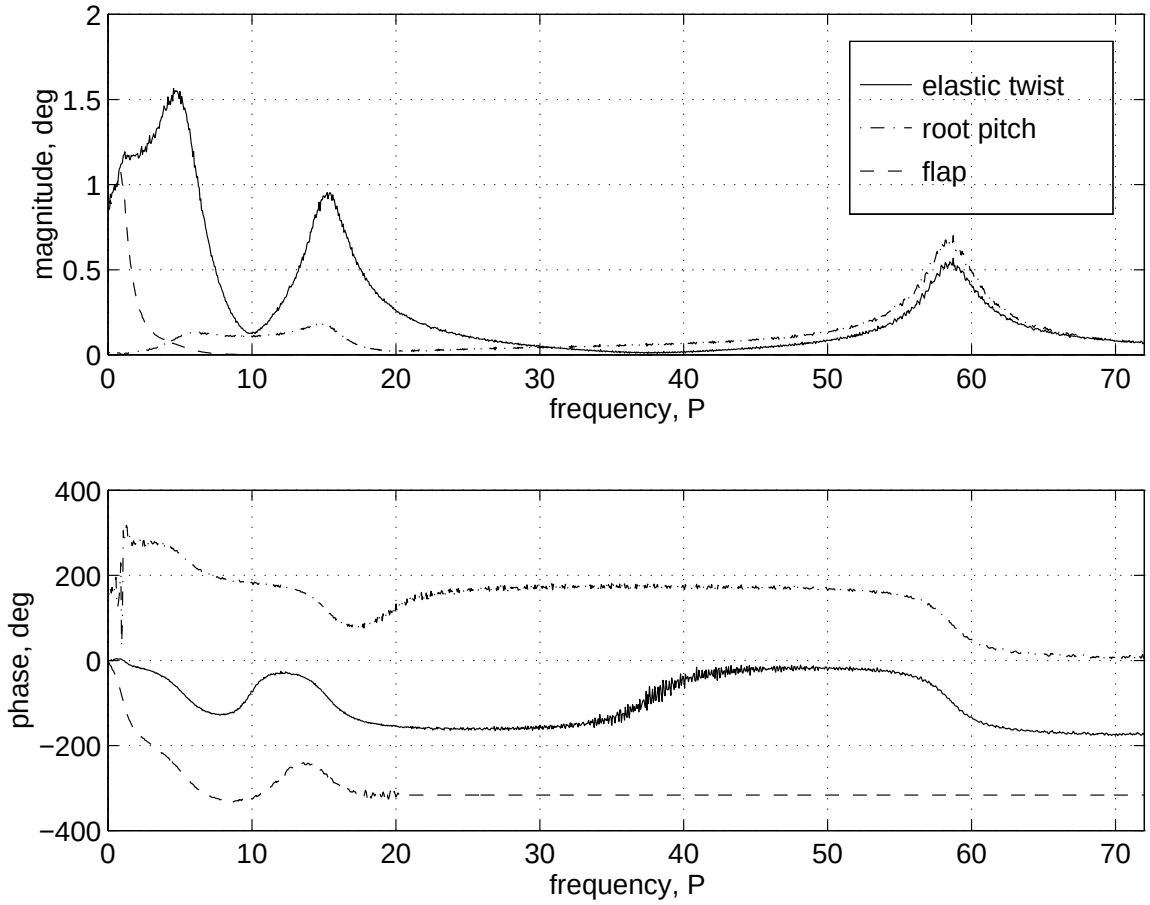

Figure 8. Blade frequency response: PFC twist actuation with interdigitated electrode poling scheme; C_T = 0.00465, μ = 0.0.

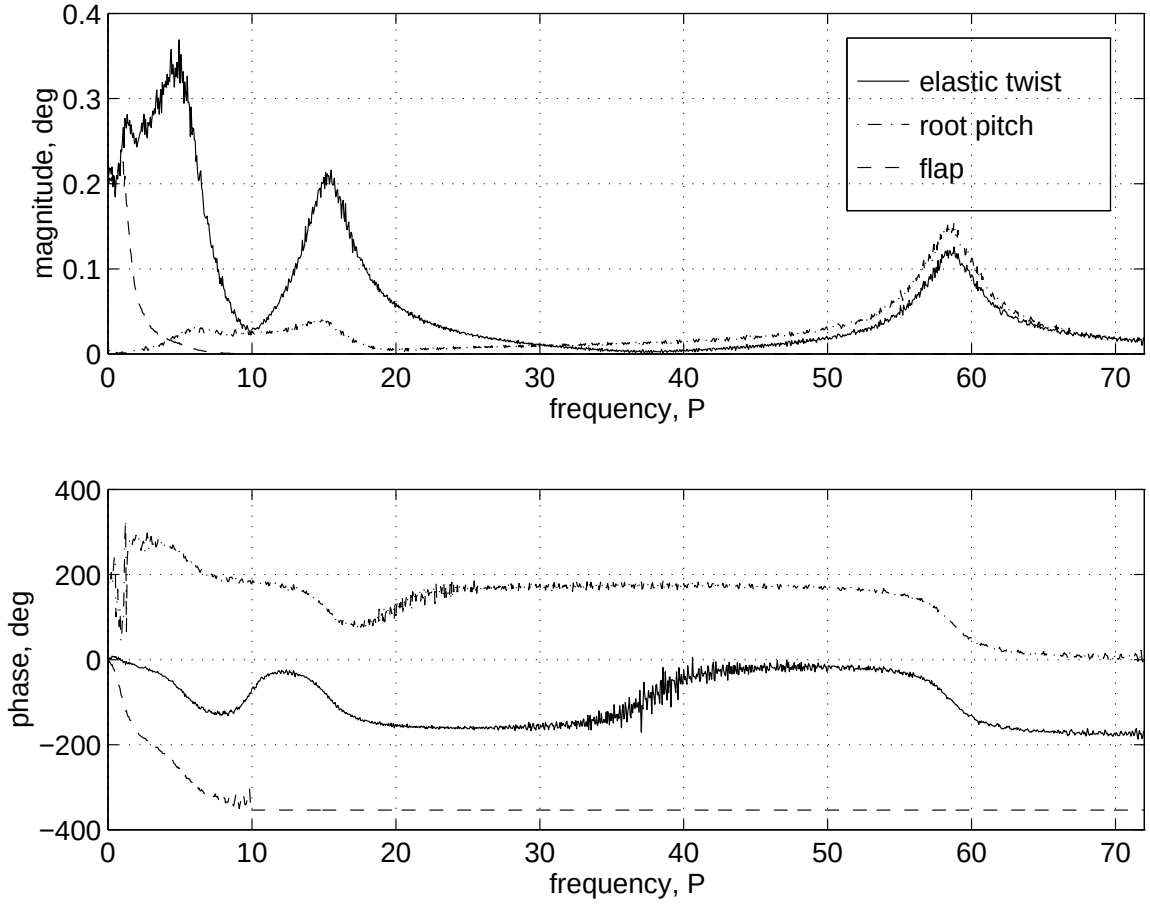

Figure 9. Blade frequency response: PFC twist actuation with conventional electrode poling scheme (DAP); C_T = 0.00465, μ = 0.0.

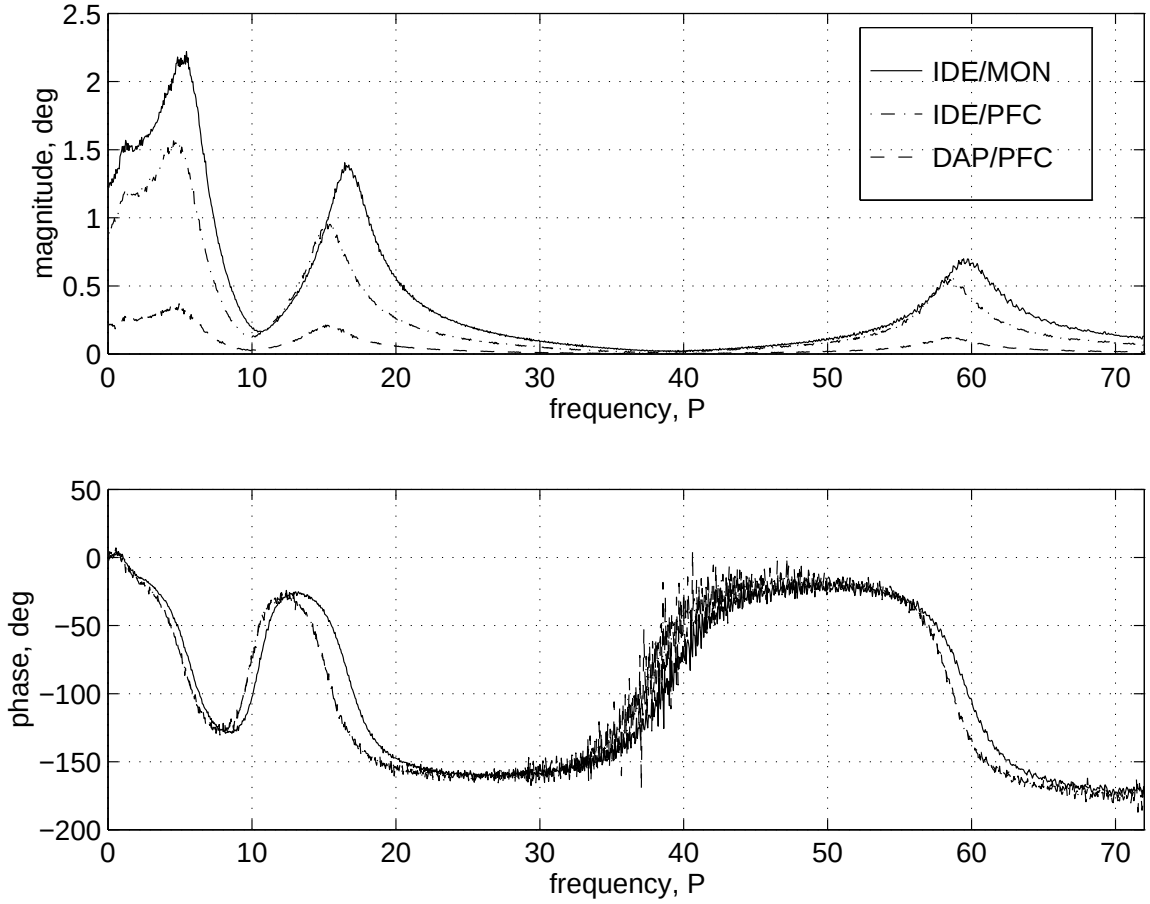

Figure 10. Comparison of elastic twist frequency response for IDE/MON, IDE/PFC, and DAP/PFC actuation schemes; C_T = 0.00465, μ = 0.0.

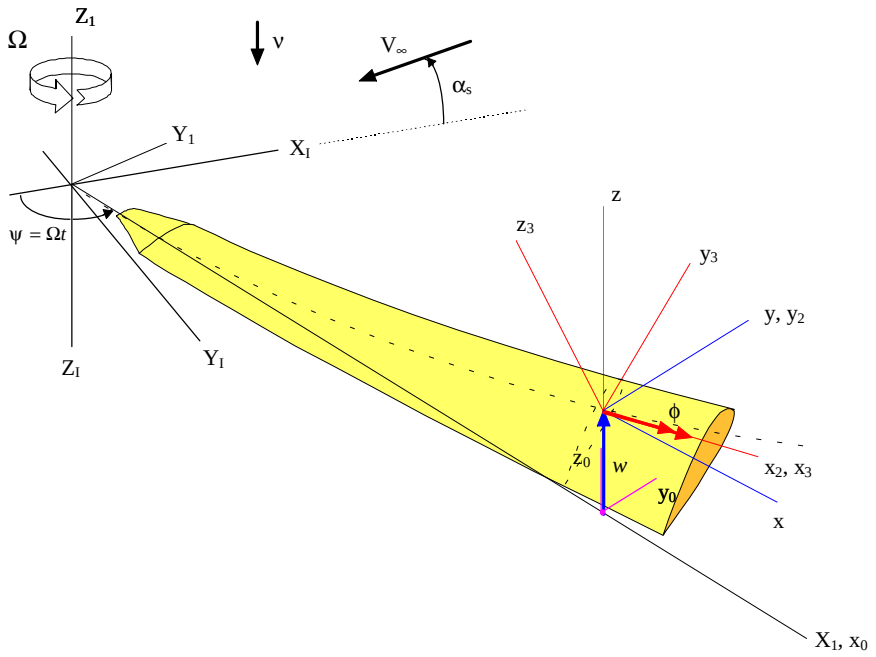

Figure A1. Rotor blade coordinate systems. Note that the blade undeformed elastic axis lies along X_1. (Section pitch angle, θ, is not shown.)

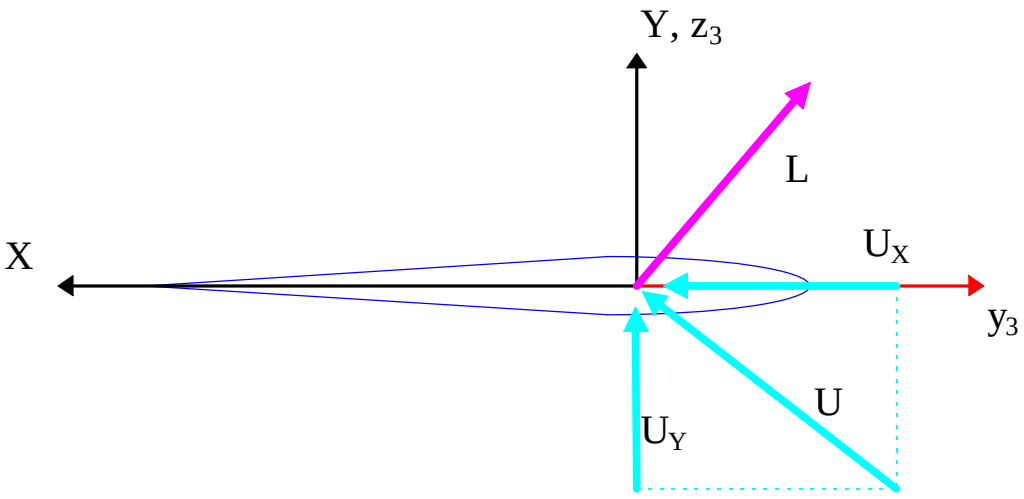

Figure C1. Airfoil section coordinate system.

REPORT DOCUMENTATION PAGE

Form Approved
OMB No. 0704-0188

1. AGENCY USE ONLY (*Leave blank*)	2. REPORT DATE	3. REPORT TYPE AND DATES COVERED
	May 1996	Technical Memorandum

4. TITLE AND SUBTITLE
An Aeroelastic Analysis of Helicopter Rotor Blades Incorporating Piezoelectric Fiber Composite Twist Actuation

5. FUNDING NUMBERS
505-63-36-02

6. AUTHOR(S)
W. Keats Wilkie
K. C. Park

7. PERFORMING ORGANIZATION NAME(S) AND ADDRESS(ES)
NASA Langley Research Center
Hampton, VA 23681-0001
Vehicle Structures Directorate
U.S. Army Research Laboratory
NASA Langley Research Center, Hampton, VA 23681-0001

8. PERFORMING ORGANIZATION REPORT NUMBER

9. SPONSORING / MONITORING AGENCY NAME(S) AND ADDRESS(ES)
National Aeronautics and Space Administration
Washington, DC 20546-0001 and
U.S. Army Research Laboratory
Adelphi, MD 20783-1145

10. SPONSORING / MONITORING AGENCY REPORT NUMBER
NASA TM-110252
ARL-MR-328

11. SUPPLEMENTARY NOTES

12a. DISTRIBUTION / AVAILABILITY STATEMENT
Unclassified - Unlimited
Subject Category 05

12b. DISTRIBUTION CODE

13. ABSTRACT (*Maximum 200 words*)

A simple aeroelastic analysis of a helicopter rotor blade incorporating embedded piezoelectric fiber composite, interdigitated electrode blade twist actuators is described. The analysis consist of a linear torsion and flapwise bending model coupled with a nonlinear ONERA based unsteady aerodynamics model. A modified Galerkin procedure is performed upon the rotor blade partial differential equations of motion to develop a system of ordinary differential equations suitable for numerical integration. The twist actuation responses for three conceptual full-scale blade designs with realistic constraints on blade mass are numerically evaluated using the analysis. Numerical results indicate that useful amplitudes of nonresonant elastic twist, on the order of one to two degrees, are achievable under one-g hovering flight conditions for interdigitated electrode poling configurations. Twist actuation for the interdigitated electrode blades is also compared with the twist actuation of a conventionally poled piezoelectric fiber composite blade. Elastic twist produced using the interdigitated electrode actuators was found to be four to five times larger than that obtained with the conventionally poled actuators.

14. SUBJECT TERMS
Helicopters, Piezoelectric Actuation, Aeroelasticity, Adaptive Structures

15. NUMBER OF PAGES
63

16. PRICE CODE
A04

17. SECURITY CLASSIFICATION OF REPORT	18. SECURITY CLASSIFICATION OF THIS PAGE	19. SECURITY CLASSIFICATION OF ABSTRACT	20. LIMITATION OF ABSTRACT
Unclassified	Unclassified	Unclassified	